

Probing the Atmospheres of Young Long-Period Sub-Neptune Progenitors with ELT/ANDES

Spandan Dash^{1*}, Dwaipayan Dubey^{2,3*}, and Liton Majumdar^{4,5}

¹ Université Paris Cité, Institut de Physique du Globe de Paris, CNRS, 1 rue Jussieu, 75005 Paris, France
e-mail: dash@ipgp.fr; dashspandan@gmail.com

² Universitäts-Sternwarte, Fakultät für Physik, Ludwig-Maximilians-Universität München, Scheinerstr. 1, D-81679 München, Germany
e-mail: ddubey@usm.lmu.de; 2014dwaipayan@gmail.com

³ Exzellenzcluster ‘Origins’, Boltzmannstr. 2, D-85748 Garching, Germany

⁴ Exoplanets and Planetary Formation Group, School of Earth and Planetary Sciences, National Institute of Science Education and Research, Jatni 752050, Odisha, India
e-mail: liton@niser.ac.in; dr.liton.majumdar@gmail.com

⁵ Homi Bhabha National Institute, Training School Complex, Anushaktinagar, Mumbai 400094, India

Received ; accepted

ABSTRACT

Context. High-resolution cross-correlation spectroscopy (HRCCS) has emerged as a powerful technique for detecting and characterizing exoplanet atmospheres from the ground. While it has been highly successful for ultra-hot Jupiters and hot Jupiters, next-generation facilities such as ELT/ANDES will extend its reach to smaller and longer-period planets, including young sub-Neptunes and their progenitors.

Aims. We investigate whether HRCCS with ELT/ANDES can robustly recover orbital parameters and atmospheric signals of the long-period sub-Neptunes V1298 Tau b and TOI-451 c. For long-period systems, the slow Doppler drift of the planetary signal over a single night reduces its separation from quasi-stationary telluric contamination, increasing the risk of signal removal during detrending. We therefore quantify the impact of including out-of-transit exposures on signal recovery and parameter estimation.

Methods. We simulate transmission observations in the YJH bands using the Ratri pipeline and analyze them with the HRCCS detrending and cross-correlation framework Upamana. For V1298 Tau b, we inject atmospheric signals consistent with HST, Spitzer, and JWST constraints. For TOI-451 c, we explore models spanning sub-solar to super-solar C/O ratios to assess compositional sensitivity.

Results. We find that incorporating out-of-transit exposures significantly enhances detectability, provided that the detrending effects are consistently propagated to the template models prior to cross-correlation. Without this reprocessing step, recovered orbital parameters can deviate substantially from injected values or yield reduced detection significance. For V1298 Tau b, $> 5\sigma$ detections of H₂O, H₂S, and CO are achievable within ≤ 10 hours (minimum two nights). For TOI-451 c, distinguishing sub-solar from super-solar C/O ratios requires ≥ 18 hours (minimum four nights). HRCCS with ELT/ANDES will therefore be a key tool for probing the atmospheric diversity of young, long-period sub-Neptunes in the ELT era.

Key words. planets and satellites: atmospheres – planets and satellites: individual: V1298 Tau b – techniques: spectroscopic – methods: theoretical

1. Introduction

Starting from the first detection of orbital motion in transmission of the hot-Jupiter HD 209458 b in 2010 (Snellen et al. 2010), the high-resolution¹ cross-correlation spectroscopy (HRCCS) technique has become a complementary tool to lower-resolution space-based observations to characterise exoplanetary atmospheres. This technique takes advantage of the fact that the exoplanetary signal during a night of observation is Doppler-shifted appreciably in wavelength space over time (a few kms⁻¹) to stand out from the photon-dominated noise (in which it is embedded) left over after all other contributions to the total flux received at the spectrograph, which either do not shift in wavelength space or shift at velocities lower than the instrumental velocity resolution, have been removed. Although

initially focussed on detecting single or multiple molecular and atomic species in the atmospheres of hot and ultra-hot Jupiters (Brogi et al. 2012; Rodler et al. 2012; De Kok et al. 2013; Birkby et al. 2013; Brogi et al. 2014, 2016; Hawker et al. 2018; Cabot et al. 2019), the development of likelihood frameworks in Brogi & Line (2019), Gandhi et al. (2019) and Gibson et al. (2020) has led to enabling of atmospheric retrievals by coupling with Bayesian parameter estimators, and thus pushed this technique into the realm of characterisation of exoplanetary atmospheres. This means that both lower-resolution space-based and high-resolution ground-based datasets for target exoplanet systems can now be analysed simultaneously to provide more precise constraints on atmospheric parameters (Brogi & Line 2019; Gandhi et al. 2019; Kasper et al. 2022; Boucher et al. 2023; Smith et al. 2024). More recently, the technique has also been utilized to either successfully detect molecules in sub-Neptune atmospheres (Basilicata et al. 2024), or to showcase the potential to detect molecules in the atmospheres

* These authors contributed equally to this work and share first authorship.

¹ $R = \lambda/\Delta\lambda > 25000$

of such exoplanets from injection tests while ultimately not detecting an equivalent signal from observed data (Lafarga et al. 2023; Dash et al. 2024; Grasser et al. 2024; Parker et al. 2025; Peláez-Torres et al. 2025). Among super-Earths, 55 Cnc e has been a consistent target for high-resolution studies (Ehrenreich et al. 2012; Zhang et al. 2021; Ridden-Harper et al. 2016; Esteves et al. 2017; Jindal et al. 2020; Taberner et al. 2020; Deibert et al. 2021; Keles et al. 2022; Rasmussen et al. 2023), but they have not resulted in any positive detections so far, while observability studies using coupled interior-atmosphere models for their spectral templates showcase that mineral atmospheres should be detectable in emission using current ground-based spectrographs like CARMENES (Dash et al. 2025). This trend of non-detection has also held true for other rocky exoplanets like GJ 486 b (Ridden-Harper et al. 2023) and GJ 1132 b (Palle et al. 2025b).

One of the most important steps of HRCCS analysis, apart from the accuracy of the template model being cross-correlated against, is the detrending procedure where all contributions to the total flux other than the Doppler-shifted exoplanet signal are removed. The two most common approaches used in literature today to perform this procedure are singular value decomposition (SVD) (first used for this purpose in De Kok et al. 2013) and SYSREM (first used for this purpose in Birkby et al. 2013). Both approaches identify the highest contributions to the flux received at spectrographs and then remove those contributions by either subtracting out the contributions to fluxes due to the first few singular/eigenvectors alone or by normalising the total flux received by those contributions. However, this process is not an unbiased approach and leads to a phase-dependant impact on line depths (attenuation) and line wing shapes (distortion) on an injected signal in the high-resolution dataset being detrended (Brogi & Line 2019; Gibson et al. 2020; Pino et al. 2022; Meech et al. 2022; Gibson et al. 2022; Cheverall & Madhusudhan 2024; Dash et al. 2024). Additionally, it also leads to production of artefacts around the injected signal, extending to all the exposures with an exoplanet signal in emission and transmission datasets (Brogi & Line 2019; Dash et al. 2024), as well as in the out-of-transit exposures for transmission datasets brought on by the detrending algorithm over-correcting at these phases due to the presence of an injected signal in the in-transit phases (Cheverall & Madhusudhan 2024; Dash et al. 2024; Palle et al. 2025a).

Presumably the detrending algorithm also has a similar effect on the actual exoplanet signal embedded in the dataset, which is why the same detrending procedure is also performed on the template exoplanet signal that is used for the cross-correlation step. The presence of out-of-transit artifacts has been shown to enhance detection significance when all detrended exposures (both in and out-of-transit) are used in the cross-correlation step, compared to using in-transit exposures alone (Dash et al. 2024; Palle et al. 2025a). These results raise the tantalizing possibility that the HRCCS may remain effective even for long-period planets in the ELT era, provided that some out-of-transit exposures are obtained during the night of observation (Cheverall & Madhusudhan 2024; Palle et al. 2025a). To evaluate this scenario, we apply an SVD-based detrending algorithm to realistic ELT/ANDES simulations of the long-period sub-Neptunes V1298 Tau b and TOI-451 c. V1298 Tau b has an orbital period of 24.139 ± 0.001 days (David et al. 2019b) and TOI-451 c has an orbital period of 9.192 ± 0.000064 days (Kokori et al. 2023). Considering both planets allows us to test the performance of the SVD-

based detrending scenario across a wide range of orbital periods.

Young sub-Neptunes such as V1298 Tau b and TOI-451 c represent an emerging class of planets whose atmospheres still retain signatures of their early formation and mass-loss histories. Both planets are part of the JWST Cycle 3 program GO 5959 (KRONOS: Keys to Revealing the Origin and Nature Of sub-neptune Systems), which targets young systems to probe how low-mass atmospheres form, cool, and undergo mass loss. Their moderate equilibrium temperatures and inflated radii make them ideal laboratories for assessing whether next-generation high-resolution spectrographs on ELT can probe atmospheric chemistry beyond the hot-Jupiter regime. V1298 Tau b, orbiting a young (< 30 Myr) pre-main-sequence K-type T-Tauri star, offers a rare benchmark with existing space-based spectra (Oh et al. 2017; Luhman 2018; David et al. 2019a; Barat et al. 2024, 2025). Initially classified as a warm Jupiter (David et al. 2019a), it was later proposed to be an inflated sub-Neptune progenitor (Kubyskhina et al. 2020; Owen 2020; Vach et al. 2024) that has not yet contracted or lost a significant fraction of its envelope. HST/WFC3 observations revealed a clear, extended atmosphere with a strong $1.4 \mu\text{m}$ H₂O feature and a large scale height (Barat et al. 2024). Follow-up observations with JWST/NIRSpec G395H revealed evidence for a haze-free, sub-solar C/O atmosphere with absorption features from H₂O, CO₂, CO, CH₄, SO₂, and OCS (Barat et al. 2025). The combined HST and JWST retrievals indicate a low metallicity, close to solar values, which is unusual when compared to mature sub-Neptunes that generally exhibit much higher heavy-element enrichments (Thorngren et al. 2016). In contrast, TOI-451 c orbits a young solar-type star with an estimated age of ~ 120 Myr (Newton et al. 2021), placing it at a later but still formative stage of sub-Neptune evolution. Its shorter orbital period and higher equilibrium temperature relative to V1298 Tau b make it an important complementary target for exploring comparative exoplanetology through atmospheric chemistry and observability analysis. Despite the absence of current space-based atmospheric constraints, its young age, inflated radius, and proximity to the host star suggest that TOI-451 c may likewise represent a sub-Neptune progenitor and hence, an exciting test case for evaluating the sensitivity of HRCCS to young, low-mass planets under more extreme irradiation conditions.

Building on this observational context, we generate forward models for both V1298 Tau b and TOI-451 c to compare their detectability with HRCCS using ELT/ANDES. For V1298 Tau b, the availability of HST and JWST/NIRSpec G395H spectra provides a direct reference for validating our high-resolution templates. In contrast, TOI-451 c currently lacks comparable atmospheric observations. We therefore explore a controlled set of atmospheric scenarios for this planet by assuming solar metallicity and three chemically plausible C/O ratios (solar, sub-solar, and super-solar). This design captures the expected diversity of atmospheric compositions for young sub-Neptunes and enables us to quantify the sensitivity of HRCCS to chemical variation. Together, this two-planet framework provides a systematic test-bed for assessing whether SVD-based HRCCS pipelines can robustly recover atmospheric signals across a range of orbital and chemical conditions relevant to ELT-ANDES. We outline our modelling and analysis framework and discuss how each component supports our objective of evaluating SVD-based HRCCS performance for young sub-Neptunes. Section 2 describes our methodology, including the generation of chemically self-consistent atmospheric structures,

Table 1: Adopted stellar and planetary parameters for the V1298 Tau b and TOI-451 c systems used in the atmospheric structure and disequilibrium chemistry calculations. Stellar properties, orbital parameters, and planetary masses and radii are taken from the literature as indicated.

| Parameters | V1298 Tau b | | TOI-451 c | |
|--------------------------------------|-------------|-------------------------|--------------------|-----------------------|
| | Values | References | Values | References |
| $M_{\text{star}} [M_{\odot}]$ | 1.26 | Finociety et al. (2023) | 0.95 | Newton et al. (2021) |
| $R_{\text{star}} [R_{\odot}]$ | 1.43 | Finociety et al. (2023) | 0.88 | Newton et al. (2021) |
| $T_{\text{star}} [\text{K}]$ | 4941 | Finociety et al. (2023) | 5550 | Newton et al. (2021) |
| Star Rotation period [days] | 2.91 | Finociety et al. (2023) | 5.1 | Newton et al. (2021) |
| Radial velocity of system [km/s] | 16.15 | David et al. (2019a) | 19.87 | Newton et al. (2021) |
| $M_{\text{planet}} [M_{\text{Jup}}]$ | 0.075 | Barat et al. (2025) | 0.031 ^a | – |
| $R_{\text{planet}} [R_{\text{Jup}}]$ | 0.85 | Barat et al. (2025) | 0.277 | Newton et al. (2021) |
| Planet Equilibrium Temperature [K] | 677 | David et al. (2019b) | 875 | Newton et al. (2021) |
| $\log(g)^{\text{a}}$ [cgs] | 3.28 | – | 3.00 | – |
| a [au] | 0.169 | David et al. (2019b) | 0.082 | Newton et al. (2021) |
| Period [days] | 24.14 | David et al. (2019b) | 9.19 | Newton et al. (2021) |
| Distance [pc] | 108.2 | Stassun et al. (2019) | 123.74 | Stassun et al. (2019) |
| Transit Duration [hours] | 6.42 | David et al. (2019b) | 3.56 | Newton et al. (2021) |

^a The values are taken from the [Exo.MAST](#) database, as these parameters have not been reported in recent peer-reviewed studies.

the computation of line-by-line high-resolution transmission spectra, and the synthesis of ANDES observations used for the HRCCS analysis. Section 3 presents the detectability tests for both planets, compares and discusses the results obtained with the presence and absence of a reprocessing step before cross-correlation analysis (for V1298 Tau b), showcases how atmospheric chemistry can influence the recovery of injected signals and whether it is possible to differentiate between different atmospheric chemistry scenarios using our synthetic nights (for TOI-451 c). In Section 4, we conclude and state the implications of our findings on the feasibility of detecting and characterizing the population of young, low-mass, and long-period exoplanets with ANDES.

2. Methods

Figure 1 provides the overview of the modeling pipeline followed in this work. Our framework consists of three main stages. First, we compute one-dimensional radiative–convective–thermochemical equilibrium structures using `petitCODE` (Mollière et al. 2015; Mollière 2017), and then derive disequilibrium abundance profiles with the 1D chemical kinetics model `VULCAN`² (Tsai et al. 2017, 2021). Second, these profiles are used to generate high-resolution line-by-line transmission spectra with `petitRADTRANS`³ (version 3.2.0) (Mollière et al. 2019, 2020; Nasedkin et al. 2024). Third, the spectra are propagated through the high-resolution observation simulator `Ratri` (Dash et al. 2025), which incorporates stellar `PHOENIX` stellar models (Husser et al. 2013), telluric transmission, and observatory conditions. Ultimately, the resulting time series observations are analysed with the SVD + MLR-based HRCCS pipeline `Upamana` (Dash et al. 2024, 2025). The subsections below describe each component of this workflow.

² <https://github.com/exoclimate/VULCAN>

³ <https://petitradtrans.readthedocs.io/en/latest/>

2.1. Integrated Modeling of Atmospheric Structure and Disequilibrium Chemistry

The atmospheric chemistry for V1298 Tau b and TOI-451 c is carried out using a combined radiative–convective and disequilibrium-kinetics framework. The atmospheres are discretized among 160 layers on a fixed pressure grid spanning from 10^2 bar at the lower boundary to 10^{-7} bar at the top. This configuration provides sufficient vertical resolution to capture thermal gradients, chemical transitions, and vertical transport. The pressure–temperature (PT) structure of each planet is simulated using `petitCODE`, which solves for radiative–convective and thermochemical equilibrium. The radiative transfer in `petitCODE` is solved using the Feautrier method, together with Accelerated Lambda Iteration (Olson et al. 1986) and Ng acceleration (Ng 1974). These techniques significantly reduce iteration times and expedite numerical stability in atmospheres. Convection is treated through mixing-length theory, and the code iteratively updates molecular abundances, opacities, and flux profiles until radiative and convective fluxes converge at every layer. At the end, this yields a self-consistent PT structure coupled to the planet’s chemical state.

The atmosphere is constructed with the following opacity sources relevant for warm sub-Neptune atmospheres: H_2O , CO , CO_2 , CH_4 , NH_3 , HCN , H_2S , C_2H_2 (HITRAN; see Gordon et al. (2022)), PH_3 (Sousa-Silva et al. 2015), Na , K (VALD3; see Piskunov et al. (1995)), TiO (ExoMol; McKemmish et al. (2019)), and VO (ExoMol; Bowesman et al. (2024)). The treatment of Continuum opacity includes the collision-induced absorption (CIA) for H_2 – H_2 and H_2 – He pairs (Borysow et al. (1988, 1989); Borysow & Frommhold (1989); Borysow (2002); Richard et al. (2012) and H^- bound–free absorption (Gray 2008). This similar opacity treatment is also followed in recent studies (Dubey et al. 2023; Dubey & Majumdar 2024; Dubey et al. 2025). We assume cloud-free atmospheres for

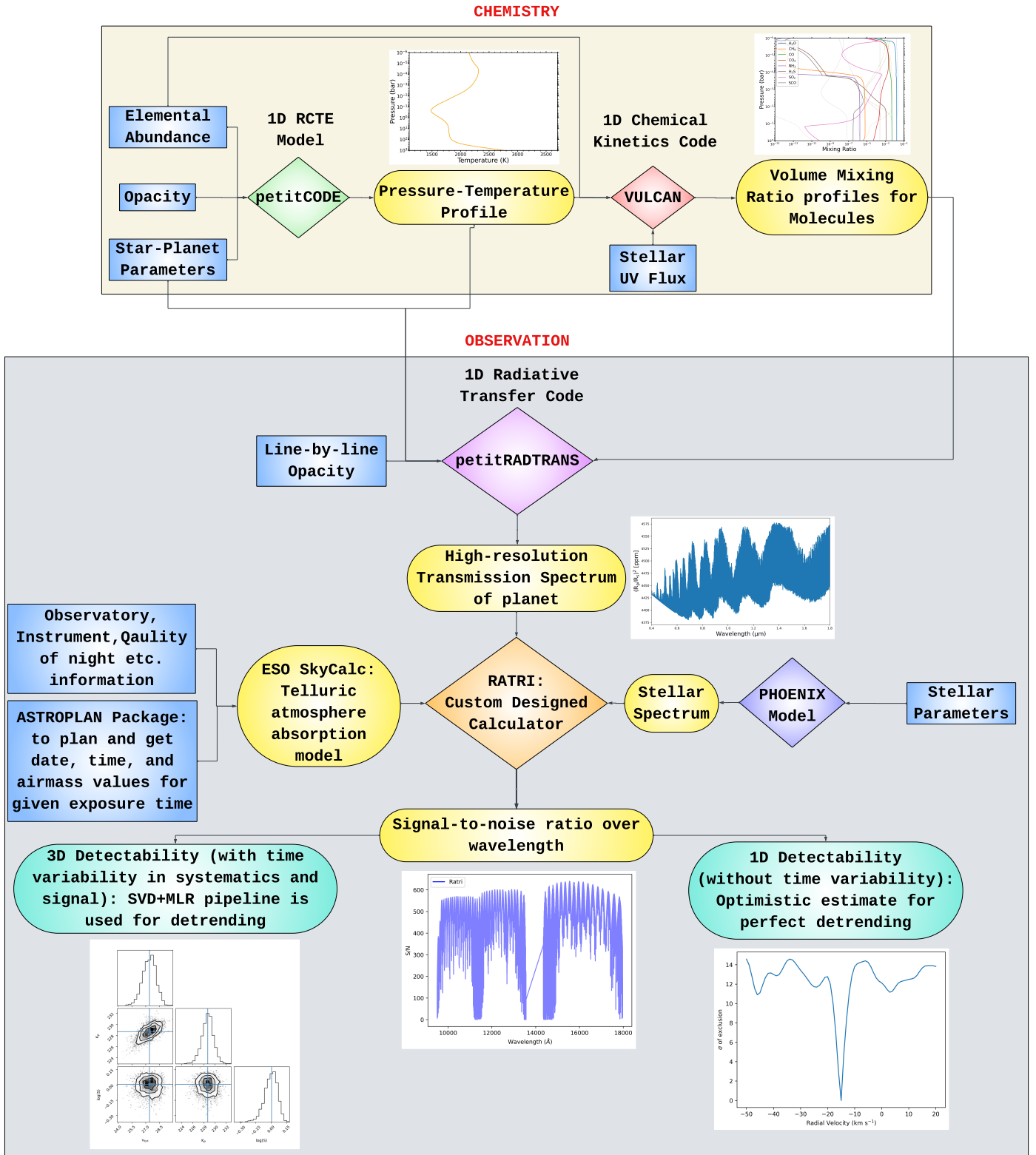


Fig. 1: Overview of the modeling and analysis workflow used in this study. The Chemistry module (top) combines elemental abundances, opacities, and star–planet parameters to compute 1D pressure–temperature profiles using 1D radiative–convective–thermochemical equilibrium model `petitCODE`, which are then coupled to the 1D chemical kinetics code, `VULCAN`, to produce volume mixing ratio profiles under stellar UV irradiation. The Observation module (middle) uses `petitRADTRANS` to generate line-by-line high-resolution transmission spectra, which are propagated through the `Ratri` ELT/ANDES simulator together with `PHOENIX` stellar models, telluric transmission from `ESO SkyCalc`, and observatory and airmass information obtained via `astroplan`. The resulting wavelength-dependent signal-to-noise ratios feed into two detectability pathways: (1) a 1D “optimistic” case assuming perfect detrending, and (2) a full 3D detectability test incorporating time-variable systematics and applying the SVD + MLR detrending pipeline. This end-to-end framework is used to assess HRCCS detectability for young sub-Neptunes in this study.

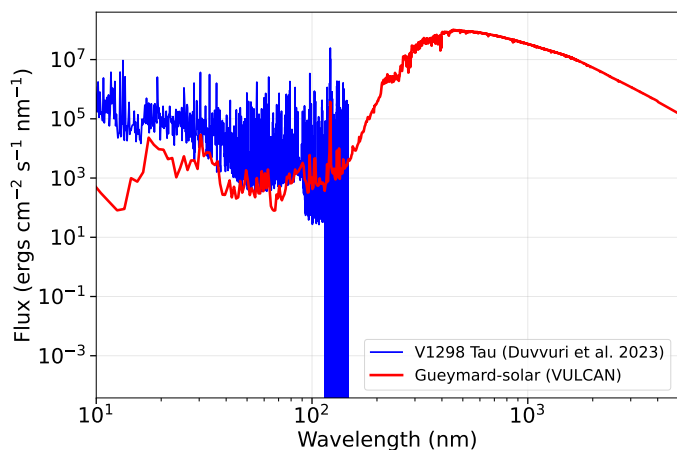


Fig. 2: Comparison of the ultraviolet stellar flux spectra used to model photochemistry in the atmospheres of V1298 Tau b and TOI-451 c. The V1298 Tau spectrum from Duvvuri et al. (2023) is rescaled to the stellar surface, whereas the “Gueymard-solar” spectrum provided with VULCAN is adopted as a proxy for TOI-451, whose effective temperature is comparable to that of the Sun.

both planets. For V1298 Tau b, this choice is supported by the HST/WFC3 observation (Barat et al. 2024), which revealed a clear atmosphere with no detectable aerosol opacity. For TOI-451 c, no observations exist to date, and adopting a cloud-free configuration keeps consistency in the comparison of chemical and high-resolution spectroscopic detectability across the two systems.

For V1298 Tau b, we model the self-consistent PT profile by implementing the retrieved atmospheric parameters from Barat et al. (2025): carbon-to-oxygen ratio $[C/O] = 0.23$ and metallicity $[M/H] = 10^{1.05}$, and internal temperature $[T_{int}] = 500$ K. Elemental abundances are assigned using the metallicity and C/O ratio prescriptions of Madhusudhan (2012); Mollière et al. (2015); Woitke et al. (2018); Molaverdikhani et al. (2019); Dubey et al. (2023); Dubey & Majumdar (2024); Dubey et al. (2025). Metallicity scales all heavy elements except H and He, and the C/O ratio is imposed by adjusting the oxygen abundance while carbon is held fixed. For TOI-451 c, since the atmosphere is not constrained from any observation, we compute different atmospheric structures assuming solar metallicity, a similar internal temperature of 500 K but spanning sub-solar, solar, and super-solar C/O ratios ($C/O = 0.22, 0.55, \text{ and } 0.80$, respectively). This design captures the expected transition from H₂O-dominated to CO-dominated to CH₄-rich thermochemical regimes.

Once the PT profiles are computed self-consistently, we integrate them to VULCAN to simulate the atmospheric chemistry under the influence of molecular diffusion, atmospheric mixing (by the implementation of Eddy diffusion coefficient) and photochemistry. A few star-planet parameters, such as Star radius, planet radius, star-planet distance, and planet gravity, are essential for calculation of disequilibrium chemistry (see Table 1). For both cases, we solve the chemistry for the “S-N-C-H-O photo network” listed in the VULCAN repository. For both planets, Eddy diffusion coefficient (K_{zz}) of 10^7 cm² s⁻¹ is implemented following Barat et al. (2025). For V1298 Tau b, the stellar ultraviolet (UV) spectrum used to model photochemistry

in the upper atmosphere is taken from Duvvuri et al. (2023). The spectrum reported in their study corresponds to the stellar flux as observed at Earth. To apply this spectrum in the context of the V1298 Tau b atmosphere, we rescaled the observed flux to the surface of V1298 Tau star using the measured distance to the system and the star radius. Since TOI-451 star has an effective temperature comparable to the Sun, we implement the “Gueymard-solar” UV spectrum from the VULCAN repository. A comparison of the ultraviolet flux profiles adopted for V1298 Tau and TOI-451 stars is shown in Figure 2. The He/H ratio is held constant at 0.085, while all other elemental abundances are scaled consistently with the metallicity and C/O ratio for each planet. Once everything is set, VULCAN computes the initial molecular abundances from its coupled equilibrium chemistry solver, FastChem⁴ (Stock et al. 2018), and then the model is iterated until the molecules converge to a steady state.

The chemical abundance profiles of the dominant species for V1298 Tau b and for three atmospheric scenarios of TOI-451 c are shown in Figure 3. For V1298 Tau b, the resulting chemical profiles are broadly consistent with the one-dimensional radiative-convective-photochemical equilibrium (RCPE) grid-chemistry retrievals for the JWST NIRSpec G395H observations (Barat et al. 2025). Notably, however, our chemistry model predicts sufficiently high abundances of SO₂ in the photospheric region to reproduce the weak absorption feature near 4.05 μm. This SO₂ signature was detected at a 4σ confidence level in free-chemistry retrievals but is not reproduced by the RCPE grid-chemistry retrieval in Barat et al. (2025). In contrast, the atmospheric composition of TOI-451 c exhibits moderate variations as a function of the assumed C/O ratio. In particular, the vertical abundance profiles of H₂O, CH₄, CO, and H₂S show the strongest sensitivity to changes in elemental composition.

2.2. Transmission spectra simulation from planet atmospheres

We compute transmission spectra for both planets by coupling time-dependent atmospheric chemistry with high-resolution, line-by-line radiative transfer. Molecular abundance profiles, obtained from VULCAN, are provided as inputs to the radiative-transfer framework petitRADTRANS⁵, where atmospheric transmission spectra are calculated relative to a reference pressure of $P_0 = 0.01$ bar. To investigate the influence of clouds on observable spectral features, we consider two idealized atmospheric configurations: a cloud-free atmosphere and a cloudy atmosphere that includes a gray cloud deck at 0.01 bar (indicated from JWST observations in Barat et al. 2025) together with a haze-like component. In the gray cloud prescription, the atmosphere is assumed to be completely opaque below the cloud deck by assigning very large opacities to deeper layers. The haze component is implemented by scaling the Rayleigh scattering cross-section of the gas by a factor of 10.

The radiative-transfer calculations include molecular opacity from species that are chemically relevant in each atmosphere. For V1298 Tau b, we consider H₂O, CH₄, CO, CO₂, NH₃, H₂S, SO₂, and SCO, while for TOI-451 c we include H₂O, CH₄, CO, CO₂, NH₃, HCN, and H₂S. Opacity data are taken from the high-resolution petitRADTRANS database or computed follow-

⁴ <https://github.com/exoclimate/FastChem>

⁵ <https://petitradtrans.readthedocs.io/en/latest/>

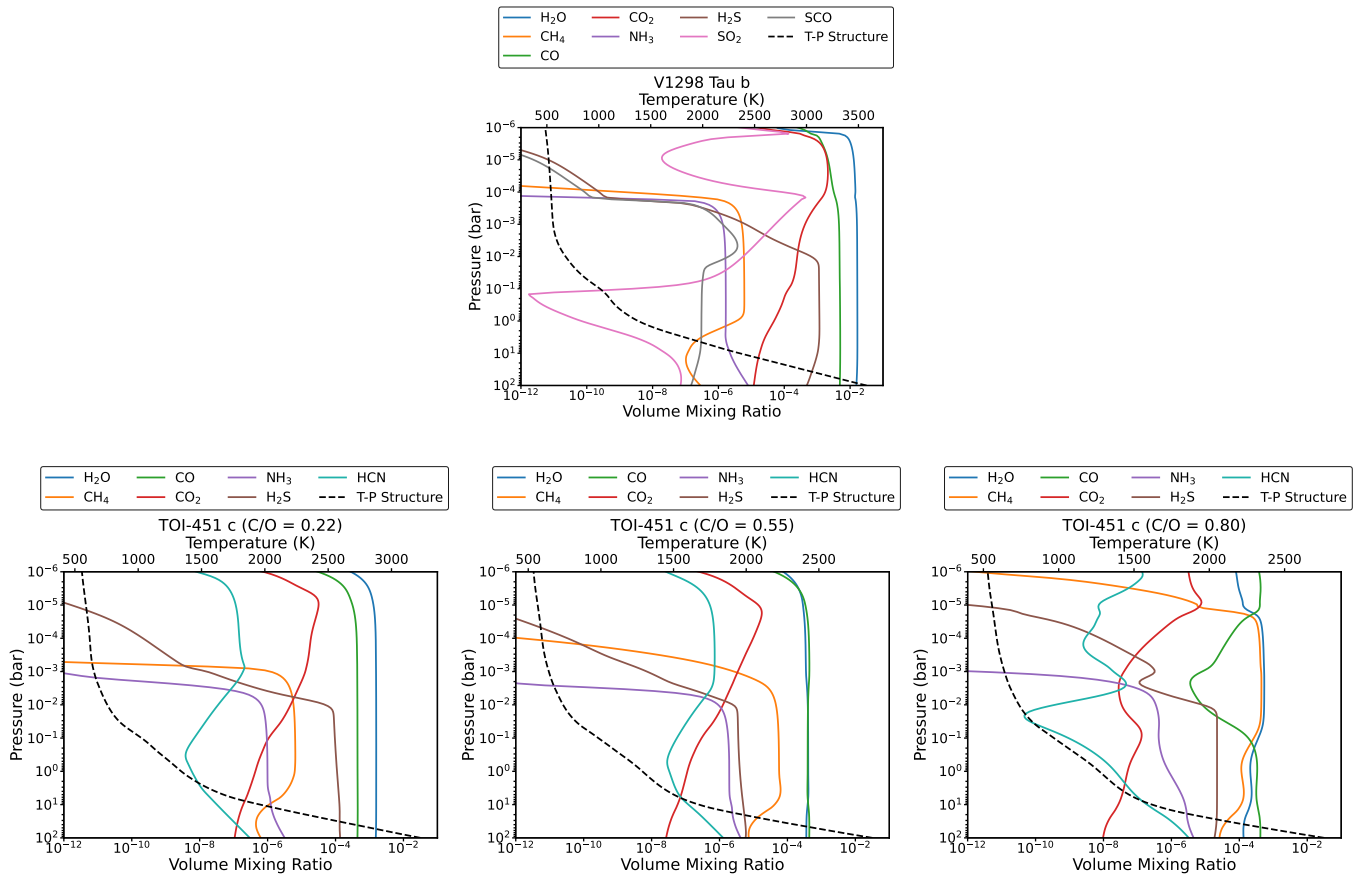


Fig. 3: Vertical chemical abundance profiles for the dominant molecular species in the atmospheres of V1298 Tau b (top panel) and TOI-451 c (bottom panels). The top panel shows the disequilibrium chemistry results for V1298 Tau b computed using a self-consistent radiative-convective pressure-temperature profile and the star-planet parameters listed in Table 1. The three bottom panels correspond to TOI-451 c models assuming sub-solar ($C/O = 0.22$), solar ($C/O = 0.55$), and super-solar ($C/O = 0.80$) elemental carbon-to-oxygen ratios at solar metallicity. All models include vertical mixing and photochemistry computed with VULCAN. The profiles illustrate the sensitivity of key species to elemental composition and disequilibrium processes across the observable atmosphere. Molecules shown are selected based on having average volume mixing ratios exceeding 10^{-8} between the 1 bar and 0.1 mbar pressure levels, corresponding to the observable photospheric region.

ing the approach described in Dubey et al. (2025). Molecules are retained only if their mean volume mixing ratio within the photospheric region (pressures between 1 bar and 0.1 mbar) exceeds 10^{-8} ; species with lower abundances are excluded as they do not contribute appreciably to the transmission spectra. In addition to molecular absorption, we include collision-induced absorption from H_2 - H_2 and H_2 -He interactions, as well as Rayleigh scattering by H_2 and He.

The intrinsic resolving power of the molecular opacity data is $R = 10^6$. In the radiative-transfer calculations, the ELT spectral resolution is incorporated through a combination of opacity sampling and instrumental convolution. The native opacities are first rebinned to the resolving power of the ELT ($R_{\text{ELT}} = 10^5$) using an opacity-downsampling factor of 10, as implemented in petitRADTRANS. The resulting spectra are then convolved with a Gaussian line-spread function, characterised by a standard deviation $\sigma_{\text{LSF}} = R/(2\sqrt{\ln 2})$, before being mapped onto the wavelength grids of ANDES. This step is essential for capturing realistic line broadening and preventing artificial enhancement of spectral contrast. To guarantee proper sampling of the instrumental resolution, we enforce the Nyquist criterion on all wavelength grids, such that $\lambda/\Delta\lambda > 2\lambda/\Delta\lambda_{\text{LSF}}$. Here, λ denotes

the wavelength at which the opacities in petitRADTRANS are defined, $\Delta\lambda$ is the wavelength spacing between adjacent grid points, and $\Delta\lambda_{\text{LSF}}$ corresponds to the full width at half maximum of the spectrograph’s line-spread function.

The resulting high-resolution transmission spectra for V1298 Tau b and TOI-451 c are shown in Figure 4. For V1298 Tau b, spectra is presented for both cloud-free and cloudy atmospheric configurations. Individual molecular contributions are shown to indicate the dominant opacity sources as a function of wavelength. For TOI-451 c, only cloud-free atmospheres are considered, and the comparison across different assumed C/O ratios illustrates how variations in elemental composition modify the relative strengths of H_2O , CO, CH_4 , and H_2S -dominated spectral regions.

2.3. Extending Ratri to ELT-ANDES

Ratri is a simulator for synthesizing nights of observations at any given date and time using high-resolution ground-based spectrographs (Dash et al. 2025). It was initially constructed to synthesize observations using the four best performing spectrographs among the currently operating ground-based

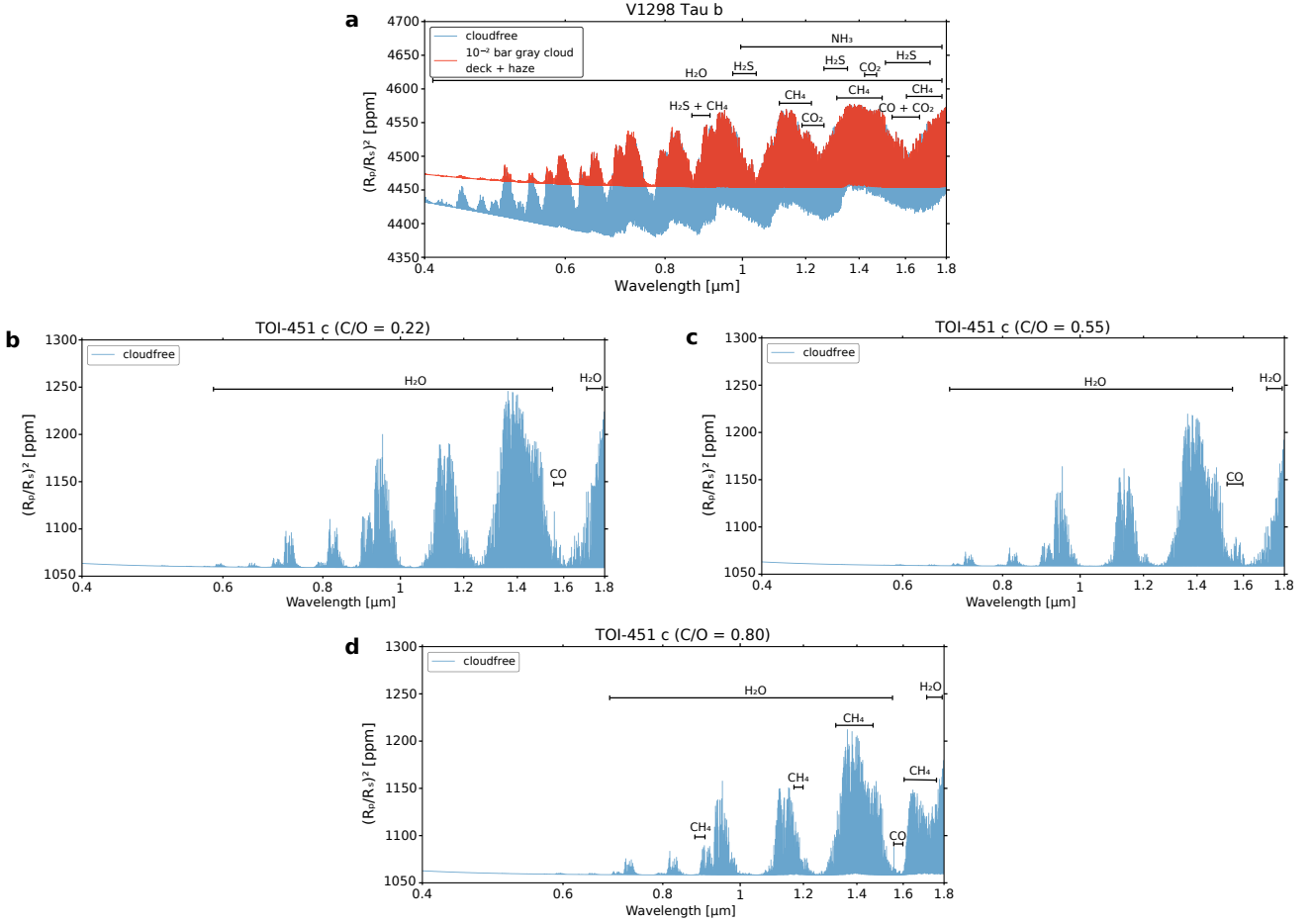


Fig. 4: High-resolution transmission spectra simulated for V1298 Tau b and TOI-451 c at the resolving power of ELT/ANDES: (a) spectrum of V1298 Tau b computed using disequilibrium chemistry and a self-consistent pressure–temperature profile, while panels (b)–(d) correspond to TOI-451 c assuming sub-solar ($C/O = 0.22$), solar ($C/O = 0.55$), and super-solar ($C/O = 0.80$) elemental carbon-to-oxygen ratios, respectively. For V1298 Tau b, cloud-free and cloudy atmospheric configurations are investigated, where the latter includes a gray cloud deck at 0.01 bar and an enhanced Rayleigh-scattering haze. All spectra include collision-induced absorption and Rayleigh scattering scaled by a factor of 10 and are convolved with the instrumental line-spread function of ANDES. The contributions of individual molecular species to the total transmission spectrum are shown as a function of wavelength.

high-resolution spectrographs - CARMENES, GIANO, SPIRou and CRIFRES+. In this study, we have extended this list to also include the ANDES spectrograph, which is scheduled to be mounted on the ELT in the future. The framework to determine the amount of flux received at the ground while taking into account the time-varying telluric absorption through Earth’s atmosphere remains the same as described in detail in Dash et al. (2025). However, we have now used a telescope of diameter 39.2 m to account for the larger collecting area of ELT. We have also included sky emission as an additional source of flux so that the resultant noise is not strictly source photon-noise, even though we operate Ratri in the photon-noise dominated regime in this study (peak SNR/resolution element per order > 300 in the YJH band). Although it is already possible to do so with the current setup of the pipeline, we have not incorporated a treatment for read-out noise (ROD) and dark-current noise, because the CCD configuration for ANDES has not yet been finalized. Additionally, with the values of dark-current noise and ROD provided in Dubey & Majumdar (2024) for ANDES, and assuming that 2 pixels are used per resolution element with an exposure time of 60 s (as will be used for V1298 Tau b in this study), the dark-current noise (i.e. the square root of

the dark-current value) per resolution element is $0.36 e^-s$, and the ROD noise is $4.2 e^-s$. Both of these terms are negligible compared to the source photon-noise value which is $> 300 e^-s$ at its lowest and about $600 e^-s$ at its highest, except in the most telluric saturated pixels which will all be masked out during the detrending procedure, and hence can be safely neglected for our feasibility simulations. We use information about efficiencies and telescope throughput available online from the ANDES Exposure Time Calculator (ANDES-ETC) (Sanna et al. 2024; Palle et al. 2025a)⁶. However, not all values were provided at the ANDES operating resolution of 100,000, so we interpolated all values on to a standardized wavelength grid of 100,000 for each wavelength band in which ANDES is expected to be operational (UBV, RIZ, YJH and K) using nearest neighbour interpolation. We compare the time-invariant (for a single airmass value of 1.2) Signal-to-Noise Ratio (SNR) per resolution element output of Ratri against the output from the ANDES exposure time calculator for 60 s of exposure of V1298 Tau in Appendix A and find reasonable agreement across all the available wavelength bands, with Ratri providing slightly higher values overall

⁶ ETC available at: <https://andes.inaf.it/instrument/exposure-time-calculator/>

across all bands with the highest values of $R_{\text{atm}} \sim 1.1 \times$ the highest values from ANDES-ETC, while reproducing the same trend of SNR variation overall. Any differences could be because R_{atm} works with a distance based framework, uses PHOENIX stellar models as default, and uses modelled telluric absorption from ESO SkyCalc (Noll et al. 2012; Jones et al. 2013), whereas the ANDES-ETC works with a stellar magnitude based framework, uses Pickles stellar spectra library (Pickles 1998), and uses the TAPAS framework (Bertaux et al. 2014) to calculate atmospheric transmission.

The ANDES-ETC does not provide spectral orders versus pixel array grids to mimic the CCD configuration, while information about the starting and ending wavelengths for each order is provided. Thus, for ease of calculation, we decided to interpolate all efficiencies and throughput values on to the YJH band CCD configuration of CARMENES, which covers almost the same wavelength range as ANDES, and is already included in R_{atm} . We only needed to scale up the size of the resolution element to be the same as that of ANDES to be able to find very similar SNR/resolution element values that we find for a standardized grid through the process outlined in the preceding paragraph. We note that CARMENES has 28 spectral orders and 4096 pixels, while the order-wise information in ETC-ANDES shows that ANDES can have double the number of orders. Since the detrending procedure itself is not spectrograph dependent, especially for ultra-stable spectrographs like CARMENES and (hopefully) for ANDES as well, we do not expect much differences in the processing step between our approach here and with future realistic observations. However, the wavelength coverage within orders and the number of pixels/resolution element can differ across the instruments, with CARMENES being sparser in comparison, which means that the trend of SNR/resolution element can vary. Consequently, the finer wavelength coverage in ANDES can result in higher values of the cross-correlation function (with more line cores of the template model available to be included in this step) compared to what we show in this study. Thus, the results of this study should be taken as a conservative estimate compared to results from actual observations in the future. Having spectral orders versus pixel array grids makes it easy to synthesize flux cuboids of dimensions $n_{\text{orders}} \times n_{\text{spectra}} \times n_{\text{pixels}}$, where n_{orders} is the number of spectral orders (28 for CARMENES), n_{spectra} is the number of exposures taken during the night of observation, and n_{pixels} is the number of pixels (4096 for CARMENES) as a proxy for the wavelength. For finding the number of exposures, based on total observation time, we also assume a read-out time of 34 s between exposures (same as CARMENES), which is slightly higher than the 30 s used in Palle et al. (2025a).

Once the flux cuboids have been prepared, the time-varying exoplanet signal is injected into the cuboids. For this, we first normalize the template spectrum prepared in Section 2.2 to their continuum, and then this normalized spectrum is Doppler-shifted in time corresponding to the exoplanetary parameters found in literature (see Table 1). The Doppler-shifted spectrum is injected into each of the exposures through the equation:

$$F_{\lambda, \star+P} = F_{\lambda, \star} \left[1 - \left(\frac{R_{\lambda, P}}{R_{\star}} \right)^2 \right]. \quad (1)$$

Here, $F_{\lambda, \star+P}$ is the combined wavelength dependent stellar and exoplanet photon flux for each exposure, $F_{\lambda, \star}$ is the wavelength dependent stellar photon flux, and $\left(\frac{R_{\lambda, P}}{R_{\star}} \right)^2$ are the wavelength de-

pendent transit depths calculated in Section 2.2 where $R_{\lambda, P}$ is the wavelength dependent radius of the exoplanet and R_{\star} is the stellar radius. The addition of white noise and instrumental effect is as described in Dash et al. (2025), and the resultant photon flux cuboid thus obtained is denoted as \mathbf{A} . These photon flux cuboids are the starting points for most HRCCS analyses in literature.

2.4. HRCCS analysis using Upamana

To detect the exoplanet signal embedded in \mathbf{A} , we need to remove all sources of photon flux other than the time varying exoplanet signal. The HRCCS detrending and analysis pipeline Upamana (Dash et al. 2024, 2025) achieves this by removing all sources of photon flux variations that do not vary in time (or vary at velocities lesser than the velocity resolution of the spectrograph) across wavelength by using a singular value decomposition (SVD)+multi-linear regression (MLR) based framework. This detrending procedure is ideally not supposed to remove the exoplanet signal within the first few highest ranked singular vectors because such a (weak) signal is Doppler shifted across wavelength due to the orbital motion of an exoplanet at a few km s^{-1} (greater than the instrumental velocity resolution) throughout an observation. Thus, after detrending the flux cuboid, the exoplanet signal represents a time varying source of flux variation buried in the white noise, which can then be analysed using a cross-correlation analysis. The methodology behind the pre-processing and detrending procedures and the subsequent cross-correlation analysis utilized in Upamana has been described in detail in Dash et al. (2024) and Dash et al. (2025), but we include a brief description below for convenience.

2.4.1. Preprocessing through low flux masking

We preprocess \mathbf{A} by masking out the low S/N pixels and the pixels with the most strongly saturated telluric absorption features, and set their values to 0 so that they don't interfere with the detrending process. We perform this step on each $n_{\text{spectra}} \times n_{\text{pixels}}$ array (so order-wise) by setting a minimum flux threshold of 5 percent of the median of the highest 300 flux values in that spectral order (same threshold used in Dash et al. (2024)). From here on, all subsequent analyses are assumed to be done order-wise as above unless stated explicitly otherwise. To keep track of all the matrices involved in this section from here on, we also provide Table 2.

2.4.2. Standardisation and Detrending

The variations in flux rather than absolute flux values are what ultimately matter to Upamana. Thus, we standardize \mathbf{A} (order-wise) by equalising the contributions from any large scale features that can contribute highly to flux variation by subtracting the array of flux values across time (i.e. for all exposures) for each pixel (i.e. each wavelength value) by their mean, and then dividing all the mean-subtracted flux values by the standard deviation of the array of flux values before they were mean subtracted. This leaves us with the standardized matrix \mathbf{A}_S where the weights for flux data over each pixel (i.e. each wavelength) have been equalized.

Next, we detrend \mathbf{A}_S by performing a time-domain SVD/PCA decomposition followed by MLR to capture the effect of scaling of the singular vectors due to prior standardisation. All major sources of variation in \mathbf{A}_S , except for the time-varying exo-

Table 2: List of matrices used in Section 2.4

| | |
|---------------------|---|
| \mathbf{A} | Flux matrix generated from Ratri at the end of Section 2.3 |
| \mathbf{A}_S | Standardised flux matrix |
| β | Detrending matrix |
| \mathbf{A}' | Best-fit matrix to \mathbf{A} from SVD+MLR (application of β) |
| $\mathbf{A}_{N,d}$ | Detrended and normalised matrix of residuals with masking |
| \mathbf{A}_m | Matrix with an injected exoplanet signal to \mathbf{A}' |
| \mathbf{A}'_m | Best-fit matrix to \mathbf{A}_m by application of β |
| $\mathbf{A}'_{N,m}$ | Detrended, normalised and reprocessed matrix of residuals without masking |
| $\mathbf{A}_{N,m}$ | Detrended, normalised and reprocessed matrix of residuals with masking |

planet signal, are assumed to be captured with the first k highest ranked singular vectors obtained by SVD decomposition. The functional effect of this detrending procedure is equivalent to multiplying matrix \mathbf{A} by a (detrending) matrix β resulting in the best fit matrix \mathbf{A}' which contains contributions corresponding to the first k highest ranked singular vectors, as shown in Dash et al. (2024). After detrending, we are left with the matrix of residuals ($\mathbf{A}_{N,d}$) with values clustered around 1.0, which is obtained as:

$$\mathbf{A}_{N,d} = \mathbf{A}/\mathbf{A}'. \quad (2)$$

The variations from 1.0 in $\mathbf{A}_{N,d}$ are due to both white noise (in simulated datasets and all sources of noise in real datasets) and the Doppler-shifted exoplanet signal. We save \mathbf{A}' and β to reproduce the effects of the detrending analysis in this step on each forward model template used for cross-correlation to reprocess this model template. This process is extensively described in Dash et al. (2024) and is necessary as the detrending procedure has been shown to leave an impression on any embedded exoplanetary signal in the flux cuboid. This reprocessing step is performed by first injecting an exoplanetary signal by Doppler-shifting it according to some orbital solution and then using Equation 1 for each exposure in \mathbf{A}' to give the noiseless flux cuboid \mathbf{A}_m , which now has contributions from the first k highest ranked singular vectors and an additional singular vector accounting for the exoplanetary signal. \mathbf{A}_m is then multiplied by β to transfer the effect of detrending by the first k highest-ranked singular vectors only to give the best fit matrix \mathbf{A}'_m . Using equation 2 on \mathbf{A}_m and \mathbf{A}'_m leaves us with $\mathbf{A}'_{N,m}$, which is the new matrix of residuals which has variations around 1.0 due to the injected time varying exoplanet model and from any other impressions produced on the exoplanet model template due to the detrending procedure. We use the same masks as found in Section 2.4.1 on $\mathbf{A}'_{N,m}$ to have $\mathbf{A}_{N,m}$, which is the reprocessed and masked model template and is hence suitable for the cross-correlation step that comes next.

2.4.3. Cross-correlation analysis through the CCF-to- $\log(L)$ framework

We use the CCF-to-likelihood framework from Brogi & Line (2019) and Gandhi et al. (2019) to find the similarity between $\mathbf{A}_{N,d}$ and $\mathbf{A}_{N,m}$. In this framework, the likelihood (L) values are calculated using the equation:

$$\log(L) = -\frac{N}{2} \log[s_f^2 - 2SR(s) + S^2s_g^2], \quad (3)$$

where s_f^2 (data variance), s_g^2 (model variance) and $R(s)$ (cross-covariance) are defined as

$$\begin{aligned} s_f^2 &= \frac{1}{N} \sum_n f^2(n), \\ s_g^2 &= \frac{1}{N} \sum_n g^2(n), \\ R(s) &= \frac{1}{N} \sum_n f(n)g(n-s). \end{aligned} \quad (4)$$

$f(n)$ and $g(n)$ are the mean subtracted values of each row from each order of $\mathbf{A}_{N,d}$, and the corresponding row from each order from $\mathbf{A}_{N,m}$. s denotes a wavelength shift, corresponding to the Doppler-shift of the model template for each tested value of exoplanet orbital velocity, which is dependant on the particular exoplanet orbital solution used for injection in the reprocessing step in Section 2.4.2. S is the scale factor by which the model template is multiplied to find the best fit with the data. When the model can correctly represent the data and the reprocessing step is adequate to perfectly reproduce the effect of detrending on the model template, $S = 1$. For retrievals, we set S as a free parameter (as $\log(S)$ instead). The retrieved value can inform about any biases inherent to the detrending procedure itself. Similar to the assumption in Dash et al. (2025), throughout this study we set $S = 1$ as from our test retrievals we find $\log(S)$ to be very close to 0 (see Figure B.1 for an example retrieval for V1298 Tau b using the simulated nights from this study).

The exoplanet orbital solution for model injection is characterised by a $v_{\text{sys}}-K_P$ pair (see Equations 10 to 14 in Dash et al. (2025) for the relevant equations), where v_{sys} is the systemic velocity of the exoplanetary system and K_P is the exoplanet semi-amplitude velocity. Thus, in order to detect an embedded exoplanet signal, we need to isolate the $v_{\text{sys}}-K_P$ pair corresponding to the injected exoplanet model from a grid of $v_{\text{sys}}-K_P$ pairs. For the exoplanets we use as case studies, the systemic velocity of the exoplanetary system are known from literature. Thus, we subtract out this systemic value from all v_{sys} values in the grid resulting in a $v_{\text{rest}}-K_P$ grid, where v_{rest} is the rest-frame velocity of the exoplanetary system. The chosen grid range and grid spacings for the analysis of each exoplanet are all described in Section 3. With the chosen grids for each exoplanet, we first calculate a $\log(L)$ value for each $v_{\text{rest}}-K_P$ pair in the grid by using each row for each order in $\mathbf{A}_{N,d}$ and the corresponding row in the same order in $\mathbf{A}_{N,m}$. Then we sum across all rows in the order, and then sum across orders to calculate a single resultant $\log(L)$ value. The highest $\log(L)$ value within the $v_{\text{rest}}-K_P$ grid

is ideally obtained at the expected exoplanet orbital solution in the case of a detection. Then we utilize the method employed in Dash et al. (2024) to calculate the confidence interval maps via a likelihood ratio test followed by application of Wilks' theorem (Wilks 1938) for 2 degrees of freedom, corresponding to a v_{rest} and K_P pair. A signal confidently detected appears as a series of tight, concentric contours around a certain v_{rest} and K_P pair, and the rest of the parameter space disfavoured by more than 4.5σ .

3. Results and discussion

3.1. The case of V1298 Tau b

3.1.1. Nights of observations

We synthesize three nights of observations using Ratri showcasing the three different ways an observation of this exoplanet might be undertaken with ANDES. We depict the resulting airmass versus exoplanetary orbital phase for all three nights in Figure 5. Night 1⁷ is simulated for the night of 20th-21st January 2020, lasts 2.5 hours (from 0100 to 0330 hours UTC, airmass between $1.4 \rightarrow 2.0$) in total with all 96 exposures captured while the exoplanet is transiting its host star. Due to V1298 Tau b's long transit duration, there is never a case where a complete transit for this exoplanet can be captured. The exoplanetary system is also a relatively northern target, which means that the airmass does not go below 1.4 even in the periods the target would be observable from the ELT. Night 2 is simulated for the night of 24th-25th December 2030, lasts 4 hours (from 0100 to 0500 hours UTC, airmass ranging from $1.6 \rightarrow 1.4 \rightarrow 1.9$) in total and has 26 of the total 153 exposures captured happening after the exoplanet has already transited its host star. Night 3 is simulated for the night of 17th-18th December 2032, lasts 4.5 hours (from 0100 to 0530 hours UTC, airmass ranging from $1.7 \rightarrow 1.4 \rightarrow 1.9$) in total and has 55 of the total 172 exposures captured happening before the exoplanet starts transiting its host star. For all three nights, this is close to the maximum number of exposures that can be captured from the ELT site, as in extending the limits of observation we would either reach exposures where the airmass is greater than 2 (generally the limit after which the AO system does not work optimally), or is in regions where it is either astronomical twilight or the beginning of dawn. For all three nights, the exoplanetary signal is not injected in the exposures captured at times when the exoplanet is not transiting.

For the first two nights, we use a PWV (precipitable water vapour) value of 2.5 mm, while we use a value of 3.5 mm for the third night. These two values are within the 'Good' night parameters for CARMENES in Ratri, and we use them here in absence of measurements of possible PWV values at the ELT site. We note that the location at which Calar Alto, the site for CARMENES, is situated generally has higher humidities compared to Cerro Paranal (Sánchez et al. 2007), which would be closest to Cerro Armazones in terms of location. Hence, the PWV values used here should be considered to be upper limits that can be obtained during particularly humid nights during

⁷ We note that for the nights synthesized in this study, astroplan (Morris et al. 2018) used in Ratri will throw a warning indicating a dubious year. This is because the dates we are simulating for are far enough in the future that the IERS data used for calculation of Earth's orientation in the inherent astropy module are no longer valid and defaults to using a 50-year mean to do such a calculation. Thus, these dates should only be seen as indicative rather than definite.

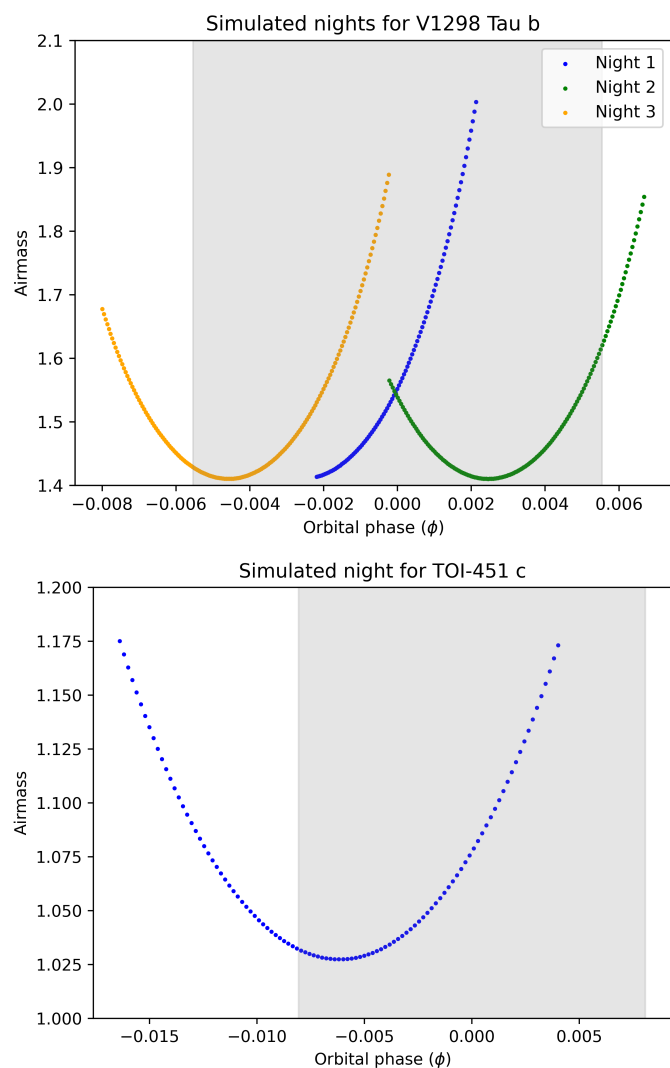


Fig. 5: The variation of airmass versus exoplanet orbital phase in simulated nights using Ratri for the case of V1298 Tau b (top panel) and TOI-451 c (bottom panel). Phases falling inside the shaded region represent in-transit phases. For more discussions about the synthetic nights, see Sections 3.1.1 and 3.2.2.

observations at the location of the ELT. We do not consider the variation of PWV with time, but note that the high-resolution detrending procedure using SVD and SYSREM is known to be very effective at removing telluric contamination (Meech et al. 2022). So, with that variation added we would expect the number of singular/eigenvectors used leading to a similar level of detrending shown in this work being higher than the values presented here. Ratri uses a high-resolution PHOENIX model to approximate the spectrum of V1298 Tau. However, this host star is a pre-main sequence star, so the PHOENIX spectrum might not be the best fit. However, in the absence of other high-resolution models for pre-main sequence stars, we decided to use PHOENIX for demonstration purposes.

3.1.2. Detectabilities

We first decided to examine if the exoplanetary signal corresponding to a cloud-free scenario for V1298 Tau b injected in our datasets is detectable or not in the optimistic scenario

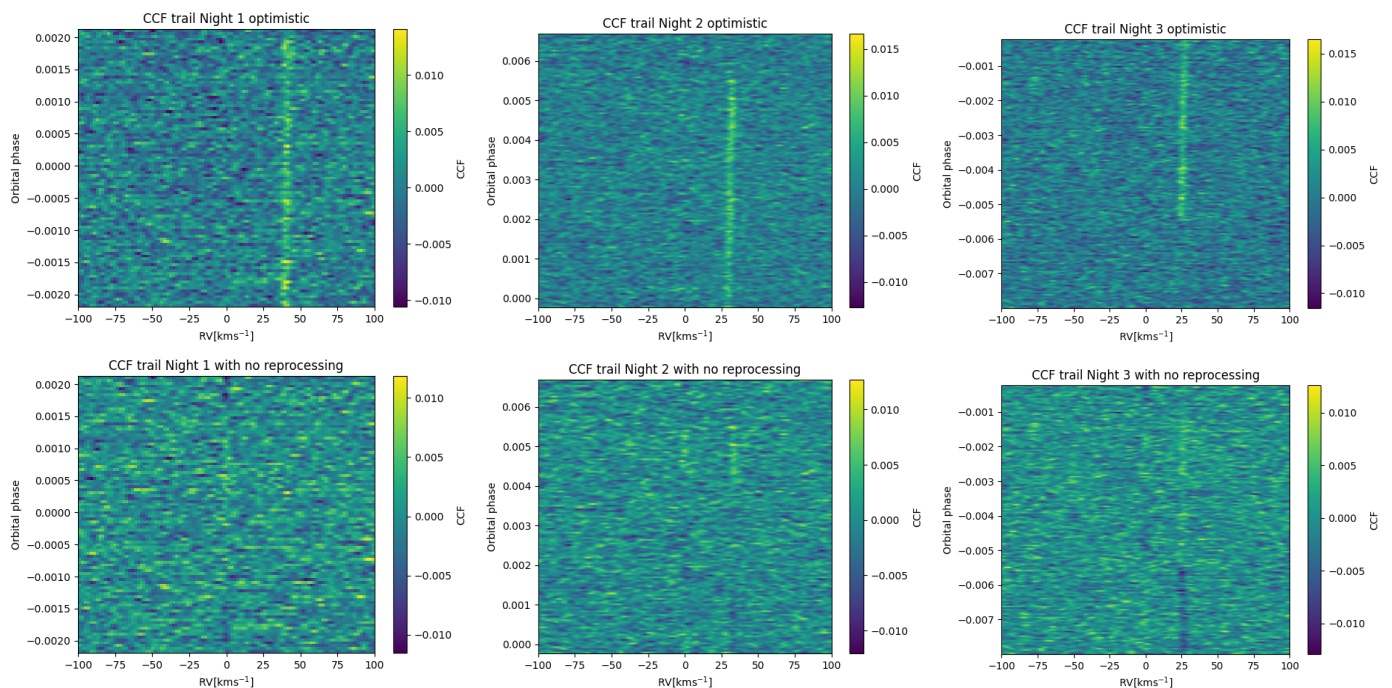


Fig. 6: Exoplanet orbital trace plots for the cloud-free case of V1298 Tau b for (top row) the optimistic detrending scenario and (bottom row) the non-reprocessing scenario where the SVD+MLR based detrending is followed by cross-correlation with a template model with no reprocessing performed on it. In the first row, the exoplanet orbital motion of V1298 Tau b tracing the the maximum of the CCF value at each orbital phase is clearly visible in the in-transit phases for each night. However, in the non-reprocessed case the CCF trail is no longer visible for the first two nights and is only faintly visible in the third night. Additionally, the third night also shows an anti-trail of negative CCF values extending in the out-of-transit phases.

when all the stellar flux and telluric contamination can be exactly removed. This is easy to do for our synthetic datasets as Ratri also produces a version of the flux cuboid with no exoplanet signal injected. Thus in the optimistic scenario, we simply divide out the synthetic flux cuboid with an exoplanetary signal with the flux cuboid with no exoplanetary signal. Then we perform the cross-correlation analysis presented in Section 2.4.3. We present the orbital phase versus the radial velocities (RV) with which the template model is cross-correlated with the detrended data in the top row of Figure 6. In all three cases, the exoplanetary orbital trail tracing the maximum of the CCF values is clearly visible for all orbital values falling within the ingress and egress values. To then represent atmospheric detections on a $v_{\text{rest}} - K_P$ grid, we vary v_{rest} between -20 and 20 km s^{-1} in spacings of 1 km s^{-1} , and vary K_P between 30 and 130 km s^{-1} in spacings of 2 km s^{-1} . The grid spacings are less than the velocity resolution of the instrument but our $\log(L)$ based significance calculation is different from the significance calculated from comparison between the in-exoplanet-trail and out-of-trail CCF distributions, which are prone to an oversampling bias when the grid spacings used are less than the velocity resolution of the instrument (Sánchez-López & Millán 2025). Here, we intentionally choose to slightly oversample to maximize sensitivity and avoid the case of the peak of likelihoods falling between two grid values. The v_{rest} grid is also smaller compared to studies in literature which use a S/N metric. Unlike the S/N metric which needs a sufficiently large grid to calculate an unbiased value of the standard deviation of CCFs away from the peak CCF to estimate the CCF noise, the likelihood calculation we use here does not need a larger grid since it calculates the significance by comparison of highest

likelihood value versus all other likelihood values in the grid, i.e., it calculates the preference of the detected set of grid values compared to the rest of the grid. We find that we can also confidently detect the the $v_{\text{rest}} - K_P$ pair for the injected exoplanetary signal for all three nights using these grids, as shown in the top row of Figure 7. However, the fact that the orbital trail is very straight (as shown in Figure 6) means that the constraints on the value of K_P (which represents the slope of the orbital trail) are weak in all three scenarios. Nevertheless, the correct value lies within the 2σ contour in all three cases. Thus, the exoplanetary signal for V1298 Tau b injected in our data is at the detectable limit using HRCCS with ANDES observations.

Next, we look at a scenario where the detrending is performed using the SVD+MLR based algorithm in Upamana, but we do not reprocess our template model before we perform the cross-correlation analysis. This kind of cross-correlation analysis were used in some of the pioneering studies in the field (see Snellen et al. 2010; Brogi et al. 2012; De Kok et al. 2013, as examples) to showcase detections in hot Jupiters, and are still used for HRCCS analyses today. We use a common value of $k = 4$ as the number of singular vectors to be used to perform our detrending. This is an ad-hoc choice and not based on any injection-retrieval studies, but we observe that detections can be found for values extending until at least $k = 10$ (no further values were tested). Additionally, we also remove the spectral orders where the telluric contamination is seen to be the highest (corresponding to spectral orders 19 and 20 for CARMENES). The orbital trace plots for this scenario are provided in the bottom row of Figure 6. In comparison to the corresponding optimistic detrending scenarios, no clear orbital trace is visible

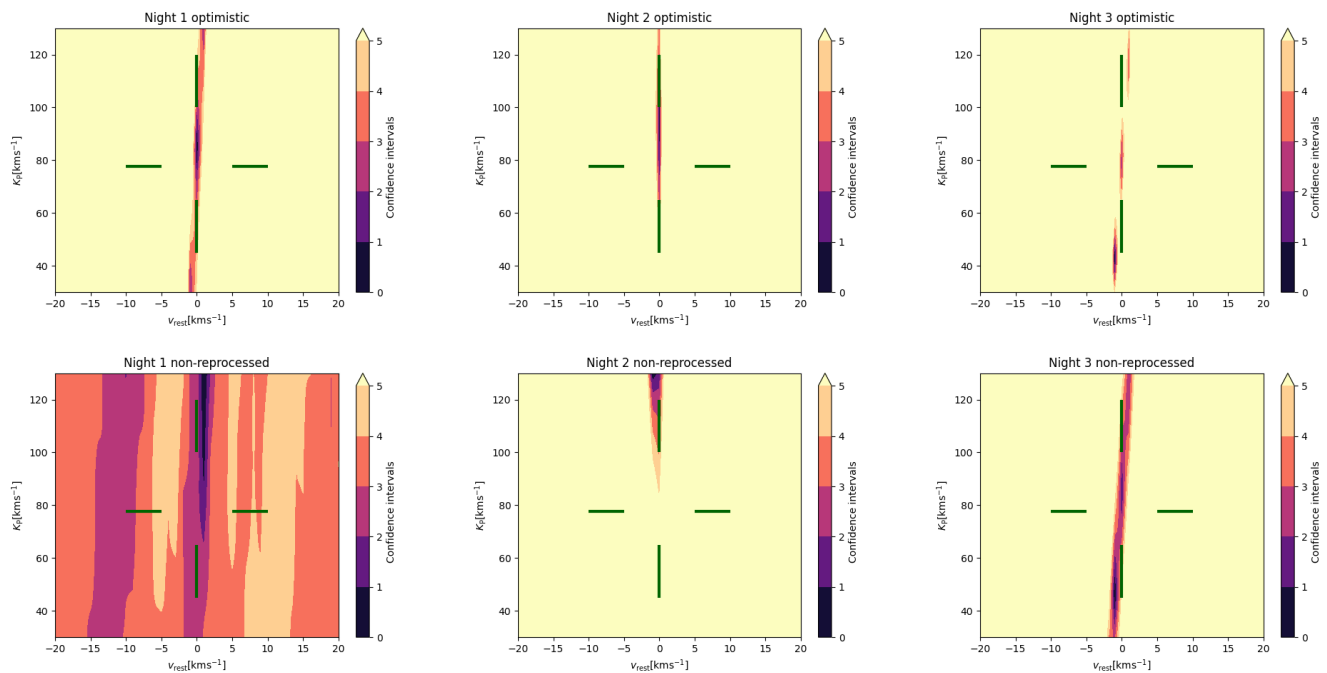


Fig. 7: Recovery of an injected signal for the cloud-free case of V1298 Tau b on a $v_{\text{rest}} - K_P$ grid for each synthetic night simulated using *Ratri* for the case of (top row) the optimistic detrending scenario and (bottom row) the non-reprocessing scenario where the SVD+MLR based detrending is followed by cross-correlation with a template model with no reprocessing performed on it. The injected signal is successfully detected in all three nights for the optimistic detrending scenario. For the non-reprocessing scenario, the injected signal is successfully detected only in Night 3 but with weaker constraints on K_P compared to the optimistic detrending case. For the other two nights, the signal is either completely removed by the detrending scenario resulting in a non-detection (Night 1) or a detection at a much higher value of K_P compared to the injected value (Night 2). For more discussion about confidence intervals and what constitutes a detection, please see Section 2.4.3.

in the first two nights. In the third night, however, the exoplanet trail is slightly visible at its expected location, but is then followed by an anti-trail of negative CCF values extending everywhere in the out-of-transit orbital phases. The presence of such out-of-transit anti-trails was also indicated by [Palle et al. \(2025a\)](#), [Cheverall & Madhusudhan \(2024\)](#) and [Dash et al. \(2024\)](#) had pointed out that the presence of an injected signal in transmission would produce out-of-transit artefacts in the out-of-transit phases after the application of a time-domain SVD based detrending procedure. The application of these artefacts is due to the inability of the detrending algorithm to properly account for the presence of an exoplanetary signal in only a few exposures, thus over-correcting for this phenomenon in the out-of-transit phases. The presence of such out-of-transit artefacts would then produce an anti-CCF trail in the out-of-transit phases if the exoplanet template is used for cross-correlation. Nevertheless, the inability to pin-point an orbital trace means that the level of detection (using only the CCF values within the ingress and egress points) varies strongly as seen in the bottom row of Figure 7. For Night 1, there is no detection at the expected orbital parameters, with the exoplanet signal presumably being almost completely removed by the SVD based detrending scenario and only resulting in a weak signature at a far-off higher K_P value. Night 2 showcases a scenario with the region indicating a strong preference for the retrieved K_P being much higher compared to the injected value. For Night 3, there is still a detection but the constraints on K_P are weaker compared to its optimistic detrending scenario counterpart.

We now look at the scenario where we run *Upamana* as usual

i.e. detrending through an SVD+MLR algorithm followed by reprocessing of the template model before the cross-correlation analysis. We retain the value of k used in the non-reprocessing case. In this scenario, since the cross-correlation analysis (including both in-transit and out-of-transit exposures) calculating the likelihood value is calculated and stored for each value in the $v_{\text{rest}} - K_P$ grid directly, we show only the resulting detection plots in Figure 8. In comparison to their non-reprocessing counterparts, Nights 2 and 3 now showcase better and more constrained detection with the injected signal parameters lying within the 2σ contours. The level of detection in Night 3 is, however, still not at the optimistic limit which means that while the reprocessing step is helpful in approximating the effect of the detrending pipeline on an injected signal, it is still not perfect. Night 1 still does not showcase a detection at the expected location on the grid, but it shows a strong unconstrained detection at a shifted v_{rest} value ($\sim -8 \text{ km/s}$). Even if this detection is due to any weak exoplanetary signature still present in the dataset, it indicates a failure of the reprocessing step to completely account for all effects of the pipeline on the injected signal. Nevertheless, the application of a reprocessing step still represents the best solution to have a detection for this exoplanet in cases where there are both in-transit and out-of-transit exposures. The level of detection in Nights 2 and 3 showcases that the proportion of out-of-transit exposures also makes a difference. [Dash et al. \(2024\)](#) reached a similar conclusion where the presence of out-of-transit spectra led to more significant detections during injection-retrieval tests. Thus, in this scenario a higher number of out-of-transit exposures will lead to more out-of-transit artefacts, which being produced by

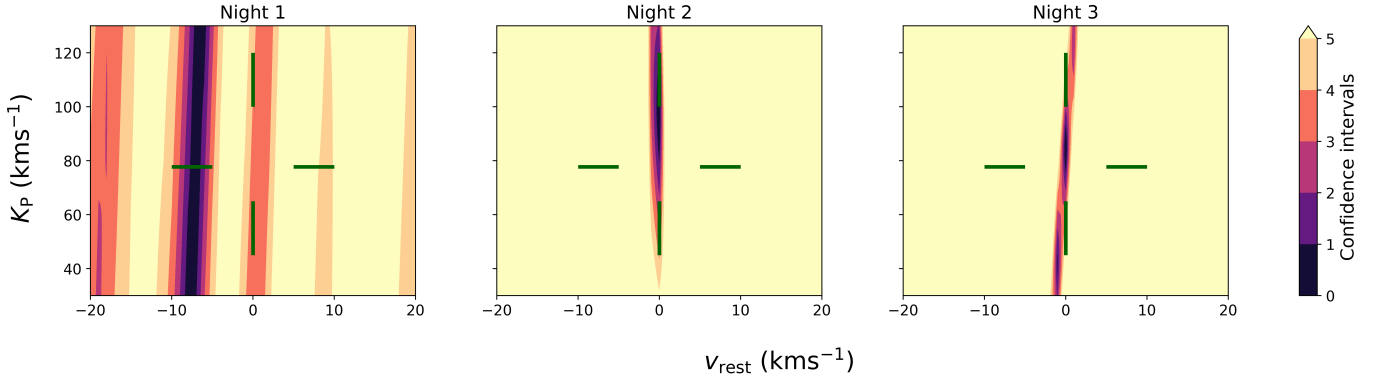


Fig. 8: Recovery of an injected signal for the cloud-free case of V1298 Tau b on a $v_{\text{rest}} - K_P$ grid for each synthetic night simulated using `Ratri` with the default reprocessing based application of `Upamana`. The injected signal is successfully detected in Nights 2 and 3 with the level of their detections better than the corresponding non-reprocessing scenarios in the bottom row of Figure 7. However, we are still not able to recover the correct parameters for the injected signal in Night 1, showcasing the limit of the reprocessing procedure when no-out-of-transit spectra are present.

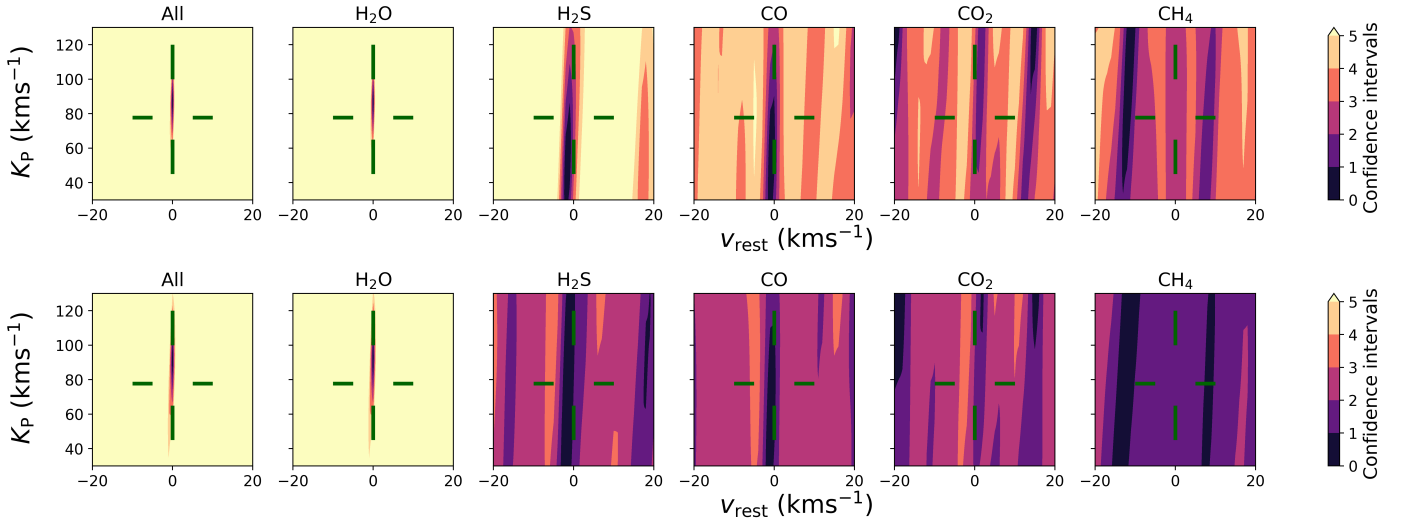


Fig. 9: Recovery of an injected signal of V1298 Tau b by combining the data from Nights 2 and 3 on a $v_{\text{rest}} - K_P$ grid with all molecules included (All) and only with individual molecules included in the template model (H_2O , H_2S , CO , CO_2 and CH_4) used for the cross-correlation analysis including the reprocessing step for the cloud-free case (top row) and with an opaque cloud deck placed at 0.01 bar (bottom row). The injected signal is successfully detected (All) in both cases with the level of their detections better than the corresponding individual night detections in Figure 8. H_2O is also detected in both cases. H_2S and CO are detected confidently only in the cloud-free case and present weak signatures in the cloud-deck scenario. CO_2 and CH_4 are not detectable in either scenario.

the presence of an exoplanetary signal in the in-transit phases also carry information about the presence of an injected signal in the in-transit phases, and hence help in pin-pointing the signal better. The reprocessing step reproduces these artefacts in the out-of-transit phases, which are also different for each value in the $v_{\text{rest}} - K_P$ grid, and accounts for their cross-correlation with the out-of-transit artefacts produced in the original detrended dataset leading to a greater likelihood value for the correct parameters.

Now that we have demonstrated that Nights 2 and 3 can be used to detect the cloud-free exoplanetary spectrum for V1298 Tau b individually, we broaden our cross-correlation analysis to check whether we can detect specific molecules - H_2O , H_2S , CO , CO_2 and CH_4 - individually, and compare them to the significance of the detection when all molecules are included to calculate the

template spectrum. Individual template spectra are calculated by repeating the procedure in Section 2.2 but then including only the opacity of the molecule, in addition to CIA absorption and Rayleigh scattering due to the presence of H_2 and He . This is equivalent to the molecule-wise analysis shown in Parker et al. (2025), and is representative of analysis done using real datasets in literature where the real exoplanetary signal has all molecules included, but the preliminary search is conducted for each molecule of interest. The results for this analysis is shown in the top row of Figure 9 on the same $v_{\text{rest}} - K_P$ grid used for the reprocessing task for each night individually. However, we have now combined the results from both nights by adding the likelihoods calculated from HRCCS analysis from each night, and then calculating the significances. As expected, combining two nights of data results in a much stronger detection and tighter constraints on the values for v_{rest} and most noticeably

K_p for the template spectrum with all molecules included, compared to each individual night in Figure 8. H_2O being an abundant molecule in the atmosphere of this exoplanet, and with a significant number of lines in the YJH band, also results in a strong detection, with the same constraints on the orbital parameters as the case with all molecules included in the template spectrum. H_2S also shows a strong detection, but with much weaker constraints on K_p . CO presents a weaker detection compared to the other molecules as most of the parameter space is excluded at $\sim 4-5\sigma$ compared to $>5\sigma$ for H_2O and H_2S . CO_2 and CH_4 show no detections, showcasing that even though they have a number of lines in the YJH band, their line depths are probably far too weak compared to the level of noise in the datasets to stand-out during the HRCCS analysis, even with two nights of observations. We note that since we used the order-wise wavelength range of the CARMENES CCD array to construct our synthetic datasets, the detections shown here represent a lower limit of the final significance achieved that can be achieved in reality as there is a difference in $0.1\mu m$ in the wavelength coverage of the H band between CARMENES (until $1.7\mu m$) and ANDES (until $1.8\mu m$).

To compare with the cloud-free results obtained above, we repeat the same analysis but now with a cloud-deck model added at the level (0.01 bar) showcased by JWST results in Barat et al. (2025). The results are shown in the bottom panel in Figure 9. There is an overall decrease in the final significance and weaker constraints on K_p compared to the cloud-free scenario for all detected molecular species, as well as the case with all molecules included in the template model. While the complete model and H_2O alone would still be easily detectable, H_2S and CO now present only weak signatures with no detections, compared to their cloud-free counterparts, because most of the parameter space is now excluded only at $\sim 3\sigma$. Dash et al. (2024) found that even weak signatures such as the ones observed here for H_2S and CO can provide constraints on the abundances of the corresponding molecules from a model selection grid. Thus, when using a complete Bayesian retrieval, similar to Gibson et al. (2022), we expect strong constraints on H_2O and the orbital parameters for V1298 Tau b, but only upper limits on the abundances for H_2S and CO. Due to time and resource constraints, that kind of retrieval is outside the scope of this work, which instead only focusses on detectability of molecular species.

3.2. The case of TOI-451 c

We use the findings from our case study of V1298 Tau b to check whether TOI-451 c, which has a much lower orbital period of ~ 9.19 days, and a transit time of 3.56 hours is also detectable using ELT-ANDES.

3.2.1. Comparative atmospheric chemistry with V1298 Tau b

To place TOI-451 c in the broader context of young sub-Neptune atmospheres, we compare its modeled chemical composition directly with that of V1298 Tau b, which benefits from existing JWST constraints. This comparison is particularly informative because both planets are young, inflated, and modeled using the same chemically self-consistent framework, yet they reside in distinct stellar and orbital environments. For one of the TOI-451 c scenarios, we adopt a sub-solar C/O ratio of 0.22, identical to the value inferred for V1298 Tau b from JWST/NIRSpec

observations (Barat et al. 2025). Despite this identical bulk C/O ratio, the resulting atmospheric chemistry differs slightly between the two planets. In particular, sulfur-bearing species such as SO_2 , which are abundant in the atmosphere of V1298 Tau b, are strongly suppressed in the corresponding TOI-451 c models. This demonstrates that elemental ratios alone do not uniquely determine atmospheric composition, especially for young sub-Neptunes where photochemistry and vertical mixing play a dominant role.

The origin of these differences can be traced to a combination of stellar irradiation and bulk atmospheric properties. V1298 Tau b orbits a very young, magnetically active pre-main-sequence star, and its photochemistry is driven by an ultraviolet (UV) spectrum derived from MUSCLES observations, which retains a comparatively high spectral resolution. This UV field enhances photolysis rates across specific molecular absorption bands and efficiently drives sulfur oxidation pathways, favouring the production of SO_2 . In contrast, TOI-451 c orbits a somewhat older solar-type star with an age of ~ 120 Myr, and its photochemistry is modeled using the Sun's spectrum from the VULCAN repository, which is provided at a lower spectral resolution. The smoother, lower-resolution solar UV input reduces the effective photolysis of key sulfur-bearing precursors, limiting sulfur oxidation and leading to a chemically distinct atmosphere, even at the same C/O ratio.

Additional differences arise from the assumed bulk metallicities of the two planets (see Section 2.1), which directly affect the absolute elemental inventories available for chemical processing. Variations in gravity and atmospheric scale height further modulate the balance between chemical and transport timescales, leading to systematic differences in the vertical abundance profiles of key molecules such as H_2O , CO, CO_2 , CH_4 , NH_3 , H_2S , and SO_2 . Together, these effects highlight TOI-451 c as a chemically distinct, yet physically related, analogue to V1298 Tau b. This comparative chemistry highlights the importance of considering stellar environment and evolutionary state when interpreting atmospheric compositions of young sub-Neptunes. In this context, TOI-451 c provides a valuable test case for assessing whether high-resolution spectroscopy with ELT/ANDES can distinguish between chemically diverse young sub-Neptune atmospheres and thereby complement the population-level constraints obtained with JWST.

3.2.2. Night of observation

TOI-451 c is a southern target and would hence be observable easily from Cerro Armazones. However, the host star is comparatively further away compared to V1298 Tau, so we found and subsequently use an exposure time of 120 s to have a similar SNR/resolution element in each exposure as in the case of V1298 Tau. We used Ratri to simulate a 4.5 hour (from 0400 to 0830 hours UTC) observation using ANDES (Night 1) for the night of 31st October 2030 with the airmass variation (between 1.175 and 1.025) throughout the observation as depicted in the bottom panel of Figure 5. We have a high proportion of out-of-transit exposures (43 out of 105 total exposures) since our previous case study shows that the reprocessing procedure of Upamana works best in such a case. We were also able to find a night (over 5 hours on the night of 27th September 2031) when the complete transit could be observed, with enough time to take out-of-transit exposures before ingress and after egress, but we found that the average barycentric velocity of the Sun-Earth sys-

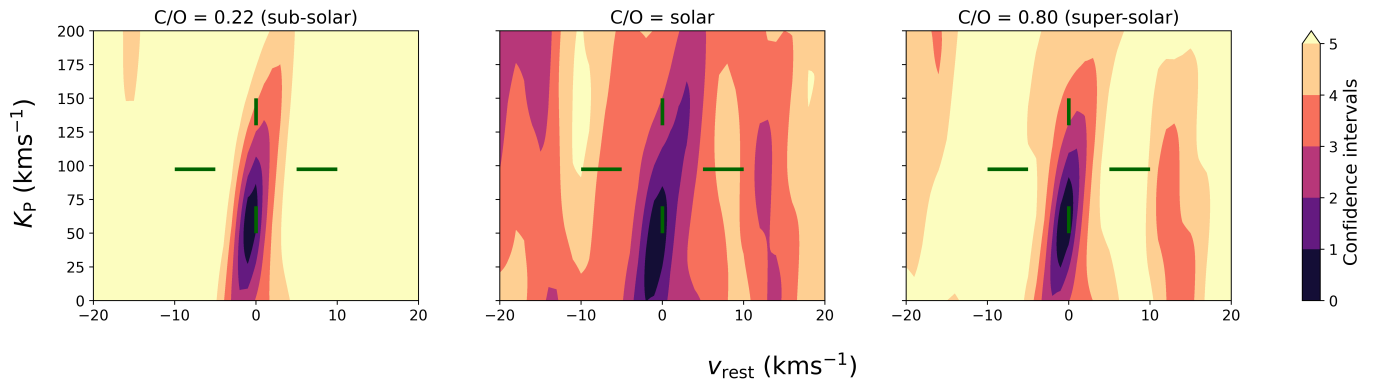


Fig. 10: Recovery of an injected signal of TOI-451 c corresponding to differing C/O ratios of 0.22 (sub-solar), 0.55 (solar) and 0.80 (super-solar) on a $v_{\text{rest}} - K_p$ grid for Night 1 (see bottom panel of Figure 5) simulated using *Ratiri* with the default reprocessing based application of *Upamana*. The sub-solar and super-solar cases are detectable, while the solar case is only marginally detectable with much weaker constraints on K_p .

tem on that date was very close in value to the systemic velocity of the exoplanetary system, which caused issues in properly detrending the dataset as lines due to the exoplanetary absorption and telluric contamination fell very close together. This is further exacerbated as the exoplanetary absorption lines are also only very slightly Doppler-shifted during the entire observation. We have included this note as a cautionary measure for any future observations when a similar phenomenon can cause issues while detrending and performing HRCCS analysis on real datasets of long-period exoplanets.

3.2.3. Detectabilities and differentiability

We first examine the detectability of TOI-451 c by assuming three different values for the atmospheric C/O ratio, synthesizing the night of observation using *Ratiri* as in Section 3.2 with the corresponding template model injected into the dataset, and then running *Upamana* with each of these template models to perform the cross-correlation analysis. We then check if all three cases would be differentiable from each other. For the detectability analysis, we run *Upamana* in its default mode with the reprocessing step included. This time we use $k = 8$ and remove the saturated spectral orders 8,9,18,19 and 20. Compared to the previous case study, we vary v_{rest} between -20 and 20 km s^{-1} in intervals of 1 km s^{-1} , and vary K_p between 0 and 200 km s^{-1} in intervals of 2 km s^{-1} . The results are shown in Figure 10. It is easily seen that the sub-solar case is well detectable, followed by the super-solar case. The solar case in comparison is only marginally detectable as most of the parameter space is rejected only at $\sim 3-4\sigma$. From Figure 4, the line depths for the sub-solar case are seen to be the deepest, followed by the solar and super-solar cases. This explains the easier detectability of the sub-solar case. Even though the super-solar case also has very similar line depths as the solar case, the increase in CH_4 abundance leads to an increase in the number of lines to now include H_2O , CO and CH_4 in comparison to mostly H_2O and CO dominated in the sub-solar and solar cases. This leads to an increase in the significance of detection for the super-solar case over the solar case as more lines are included in the cross-correlation process.

Now we check if the different C/O cases would be differentiable from each other. We utilize the same method applied for model differentiability in Dash et al. (2025). We first calculate three

$\log(L)$ grids, one each from cross-correlating all synthetic data cuboids with each template model, but on a much reduced $v_{\text{rest}} - K_p$ grid, with v_{rest} ranging between -5 and 5 km s^{-1} in 1 km s^{-1} intervals and K_p ranging between 50 and 150 km s^{-1} in intervals of 4 km s^{-1} (with the expected exoplanet K_p value falling in the middle of this range). The maximum likelihood obtained within this grid is saved as the corresponding $\log(L)$ value for the cross-correlation of a specific template model with the constructed flux cuboid. At the end, we are left with a 3×3 matrix of $\log(L)$ values and we calculate the significance values for each row of this matrix as outlined at the end of Section 2.4.3, but now with 3 degrees of freedom (instead of 2, since the model is also a free parameter now). This leaves with a model selection on a grid plot as shown in the left panel of Figure 11. If each injected model would be perfectly selected in each row through the cross-correlation analysis, we would be left with an auto-correlation diagonal with the other two models rejected. However, as the left panel shows, while the auto-correlation diagonal is seen, the rest of the models are not rejected at more than 1.5σ for the super-solar case and 1σ for the sub-solar case. The solar case cannot be differentiated at all but this is more to do with the fact that this case is only marginally detectable, as shown in Figure 10. This means that overall it is not possible to have precise constraints on the C/O ratio with just one night of data alone, especially if the exoplanet's atmosphere has a solar C/O ratio.

To get an approximate measure of how many nights we would need to be able to precisely retrieve just the auto-correlation diagonal while rejecting the other models for each row, we scaled up the $\log(L)$ matrix by the number of (similar quality) nights before calculating the significances. The case for co-adding 5 similar nights as Night 1 is shown in the right panel of Figure 11. Now, both the super-solar and sub-solar cases are easily differentiable from all other models, thus allowing precise constraints. However, precise constraints on the solar case are still not possible. The curious result for the solar case might be because we are scaling up likelihoods from a non-strongly detectable case, which does not add any more meaningful information with additional nights and instead simply scales up the same kind of bias the one night of dataset has. Thus, adding more diverse nights to quantify when the solar case would be first strongly detectable, and then scale up the resulting likelihoods to determine when it would be differentiable would be a

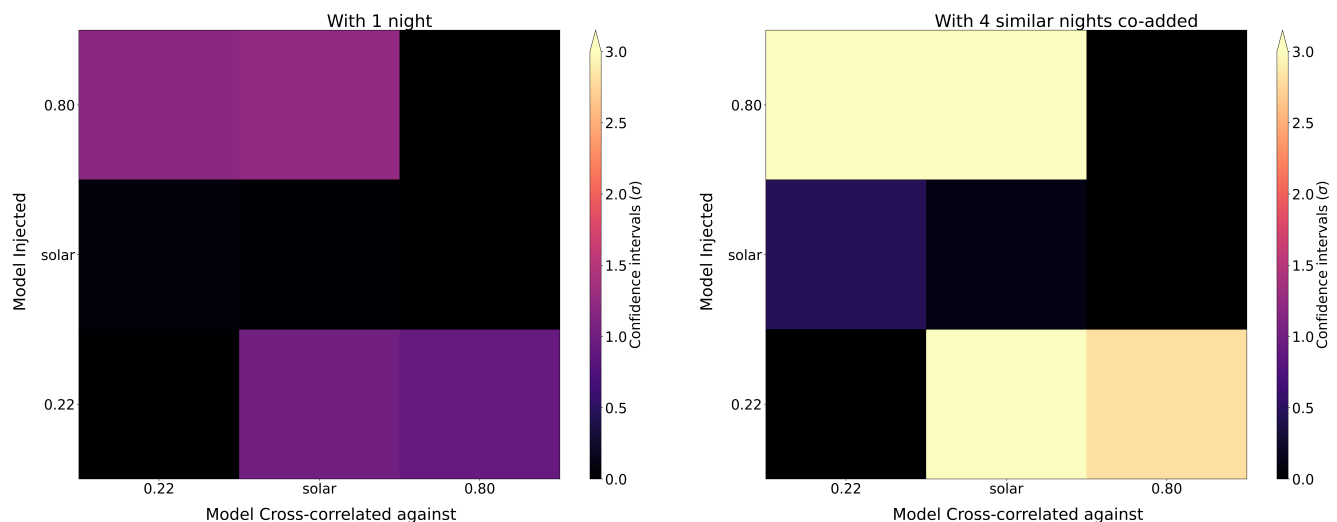


Fig. 11: Grid-based model selection plots for the case of TOI-451 c. 1 night of synthetic data (left panel) is not enough to differentiate between the diverse atmospheric C/O scenarios assumed in this study to model the atmosphere for this exoplanet. 4 nights of similar quality as Night 1 (right panel) can be used to differentiate the super-solar and sub-solar C/O cases from all other C/O cases by rejecting the models away from the auto-correlation diagonal at \sim or $>3\sigma$. However, the solar C/O case is still non-differentiable. See Section 3.2.3 for further discussion.

better strategy. However, as mentioned earlier, since this work is primarily focussed on detectability of our exoplanets, we do not proceed to make a detailed analysis regarding characterisation of C/O ratios. We simply propose that while all C/O scenarios considered here for TOI-451 c would at least be within the limits of detectability with 1 night of observation lasting 4.5 hours, it would take at least 18 hours of observations i.e. 4 nights of similar quality observations as Night 1 to constrain whether the C/O ratio of the atmosphere of TOI-451 c is sub-solar or super-solar, unless the atmosphere has a close to solar C/O ratio.

4. Conclusions

In this study, we investigated the feasibility of detecting and characterizing the atmospheres of the young, long-period sub-Neptunes V1298 Tau b and TOI-451 c at high spectral resolution with ELT/ANDES. We constructed atmospheric models informed by HST+Spitzer+JWST constraints for V1298 Tau b and explored a range of C/O ratios for TOI-451 c. High-resolution transmission templates were generated and injected into synthetic YJH-band observations produced with the Ratri pipeline. These datasets were then analyzed using an HRCCS detrending and cross-correlation framework (SVD+MLR-based) to evaluate the recovery of the injected Doppler-shifted signals and their corresponding orbital parameters. Our main conclusions are summarized below.

- We synthesize 3 nights of observations, each lasting between 2.5-4 hours, for V1298 Tau b. All three nights should have resulted in a tight detection of the exoplanetary atmosphere in the optimistic scenario, but the actual level of detection varies across the nights.
- In the night with no out-of-transit exposures, we fail to detect the exoplanetary signal whether we reprocess the template model before the cross-correlation step or not. Thus, this kind of observation represents a scenario where we expect the exoplanet signal to be almost completely eroded away by the detrending procedure. We propose that such observations be avoided for detecting and characterising long-period

exoplanets. Additionally, this also motivates future studies of better and more non-invasive ways of detrending high-resolution datasets as the current SVD/SYSREM based approaches do not let us utilise the full potential of having a larger telescope, especially for long-period exoplanets. Reprocessing is a time and resource intensive process as well, so it is worthwhile to consider alternative detrending approaches which can remove telluric contamination while not affecting the embedded exoplanet signal. Direct and more accurate modelling of telluric lines (similar to Lockwood et al. (2014)) and machine-learning approaches like one proposed in Meech et al. (2022) represent potentially attractive avenues.

- The other two nights have a significant number of out-of-transit exposures and result consistently in detections when the template model is reprocessed before cross-correlation. If the model is not reprocessed, either the obtained orbital parameters are far off from the injected values, or present less significant detections at the injected parameters. Thus, the reprocessing step is essential in HRCCS analysis with SVD/SYSREM based detrending even if the only objective is to look at predictions of detection levels across a grid of spectral templates. Failure to perform this step in such analyses might result in underestimating the overall level of detectability. Similarly, studies assuming an optimistic/perfect level of detrending for detectability and characterisation studies might overestimate the actual detectabilities. We note, however, that these results are based on a robust CCF-to- $\log(L)$ framework for calculation of significances, compared to the more widespread S/N metric or the metric for calculating detection significances based on a comparison of in-exoplanet-trail and out-of-trail distributions.
- The fact that the presence of out-of-transit exposures increases the significance of detection was investigated and proposed already in Cheverall & Madhusudhan (2024), Dash et al. (2024) and Palle et al. (2025b). Our findings are consistent with and augments the results of these studies and also

shows the drastic scenario for long-period exoplanets where the absence of out-of-transit exposures can result in non-detections, even when the exoplanet is optimistically well within the limit of detectability with the instrument. Thus, we reiterate that some amount of out-of-transit exposures be taken during observations of these exoplanets. While this study is restricted to transmission, a similar phenomenon of the exoplanet signal being present in some phases and absent in other can occur for emission spectra when the exoplanet is occulted by the star. Thus, a similar phenomenon of including in-occultation phases and out-of-occultation phases together during detrending is also worth considering (and also proposed in [Cheverall & Madhusudhan \(2024\)](#)), but a detailed analysis is beyond the scope of this study.

- For the case of V1298 Tau b, with the best fit template spectrum constructed based on the atmospheric parameters found to fit for HST+Spitzer and JWST observations in [Barat et al. \(2025\)](#), while the exoplanetary atmosphere itself is easily detectable with the YJH band of ANDES, individual molecules themselves are detected at varying significances. With two nights of synthetic observations lasting 8.5 hours in total (in which the exoplanet is detectable), we expect H₂O, H₂S and CO to be detectable. The detectability of these molecules is highest in the cloud-free case, which is expected as this case presents the deepest line depths (see Figure 4). A cloud deck case as suggested from [Barat et al. \(2025\)](#) is still detectable, but only H₂O is easily detectable in the same time-frame while H₂S and CO present weaker signatures and require more observing time to be completely detectable. The rest of molecules detected in [Barat et al. \(2025\)](#) are either not detectable in the YJH band or would require much higher observing time.
- TOI-451 c is also detectable with a single 4.5 hour of observation in the YJH band of ANDES, but the level of detectability varies between the C/O ratios assumed to model the atmospheric chemistry. The sub-solar and super-solar C/O ratio cases are more strongly detectable, with the solar C/O case being only marginally detectable. The same 4.5 hour observation is, however, not enough to be able to differentiate between these regimes, and we require at least 18 hours of observation i.e. 4 nights of similar quality as the one simulated here to differentiate between the sub-solar and super-solar cases.
- A comparative analysis of the modeled atmospheric chemistries of V1298 Tau b and TOI-451 c demonstrates that young sub-Neptunes with similar bulk C/O ratios can nevertheless exhibit different molecular compositions. In particular, sulfur-bearing species such as SO₂, which is abundant in the atmosphere of V1298 Tau b, are strongly suppressed in TOI-451 c even for the same sub-solar C/O ratio. These differences can be attributed to a combination of factors, including the contrasting ultraviolet radiation fields and spectral resolutions of the adopted stellar UV spectra, differences in assumed bulk metallicity, and variations in orbital separation and atmospheric structure. This highlights that elemental ratios alone are insufficient to fully characterise young sub-Neptune atmospheres and underscores the importance of combining JWST constraints with high-resolution ELT observations to disentangle the physical drivers of atmospheric chemistry.
- The results of this study thus suggest that not only will the HRCCS technique continue to be viable for young, long-

period sub-Neptune progenitors and sub-Neptunes themselves in the ELT era, it will also be an essential tool in characterising the diversity of this population. The long-periodicity of the results obtained here are encouraging for the case of more terrestrial exoplanets in similar or even longer period orbits as well. The detectabilities of such exoplanets need to be similarly examined in future studies.

Acknowledgements. SD acknowledges support through a Postdoctoral Fellowship from Université Paris Cité. LM acknowledges funding support from the DAE through the NISER project RNI 4011.

References

- Barat, S., Désert, J.-M., Goyal, J. M., et al. 2024, *Astronomy & Astrophysics*, 692, A198
- Barat, S., Désert, J.-M., Mukherjee, S., et al. 2025, *The Astronomical Journal*, 170, 165
- Basilicata, M., Giacobbe, P., Bonomo, A., et al. 2024, *Astronomy & Astrophysics*, 686, A127
- Bertaux, J.-L., Lallement, R., Ferron, S., Boonne, C., & Bodichon, R. 2014, *Astronomy & Astrophysics*, 564, A46
- Birkby, J., De Kok, R., Brogi, M., et al. 2013, *Monthly Notices of the Royal Astronomical Society: Letters*, 436, L35
- Borysow, A. 2002, *Astronomy & Astrophysics*, 390, 779
- Borysow, A. & Frommhold, L. 1989, *Astrophysical Journal*, Part 1 (ISSN 0004-637X), vol. 341, June 1, 1989, p. 549-555., 341, 549
- Borysow, A., Frommhold, L., & Moraldi, M. 1989, *Astrophysical Journal*, Part 1 (ISSN 0004-637X), vol. 336, Jan. 1, 1989, p. 495-503., 336, 495
- Borysow, J., Frommhold, L., & Birnbaum, G. 1988, *Astrophysical Journal*, Part 1 (ISSN 0004-637X), vol. 326, March 1, 1988, p. 509-515. NASA-supported research., 326, 509
- Boucher, A., Lafrenière, D., Pelletier, S., et al. 2023, *Monthly Notices of the Royal Astronomical Society*, 522, 5062
- Bowesman, C. A., Qu, Q., McKemmish, L. K., Yurchenko, S. N., & Tennyson, J. 2024, *Monthly Notices of the Royal Astronomical Society*, 529, 1321
- Brogi, M., De Kok, R., Albrecht, S., et al. 2016, *The Astrophysical Journal*, 817, 106
- Brogi, M., De Kok, R., Birkby, J., Schwarz, H., & Snellen, I. 2014, *Astronomy & Astrophysics*, 565, A124
- Brogi, M. & Line, M. R. 2019, *The Astronomical Journal*, 157, 114
- Brogi, M., Snellen, I. A., De Kok, R. J., et al. 2012, *Nature*, 486, 502
- Cabot, S. H., Madhusudhan, N., Hawker, G. A., & Gandhi, S. 2019, *Monthly Notices of the Royal Astronomical Society*, 482, 4422
- Cheverall, C. J. & Madhusudhan, N. 2024, *The Astronomical Journal*, 167, 272
- Dash, S., Brogi, M., Gandhi, S., et al. 2024, *Monthly Notices of the Royal Astronomical Society*, 530, 3100
- Dash, S., Brogi, M., Seidler, F. L., et al. 2025, *Monthly Notices of the Royal Astronomical Society*, 538, 3042
- David, T. J., Cody, A. M., Hedges, C. L., et al. 2019a, *The Astronomical Journal*, 158, 79
- David, T. J., Petigura, E. A., Luger, R., et al. 2019b, *The Astrophysical Journal Letters*, 885, L12
- De Kok, R. J., Brogi, M., Snellen, I. A., et al. 2013, *Astronomy & Astrophysics*, 554, A82
- Deibert, E. K., De Mooij, E. J., Jayawardhana, R., et al. 2021, *The Astronomical Journal*, 161, 209
- Dubey, D., Grübel, F., Arenales-Lope, R., et al. 2023, *Astronomy & Astrophysics*, 678, A53
- Dubey, D. & Majumdar, L. 2024, *The Astrophysical Journal*, 972, 165
- Dubey, D., Majumdar, L., Beichman, C., et al. 2025, *The Astrophysical Journal Supplement Series*, 278, 19
- Duvvuri, G. M., Cauley, P. W., Aguirre, F. C., et al. 2023, *The Astronomical Journal*, 166, 196
- Ehrenreich, D., Bourrier, V., Bonfils, X., et al. 2012, *Astronomy & Astrophysics*, 547, A18
- Esteves, L. J., De Mooij, E. J., Jayawardhana, R., Watson, C., & De Kok, R. J. 2017, *The Astronomical Journal*, 153, 268
- Finocchia, B., Donati, J.-F., Cristofari, P., et al. 2023, *Monthly Notices of the Royal Astronomical Society*, 526, 4627
- Foreman-Mackey, D., Hogg, D. W., Lang, D., & Goodman, J. 2013, *Publications of the Astronomical Society of the Pacific*, 125, 306
- Gandhi, S., Madhusudhan, N., Hawker, G., & Piette, A. 2019, *The Astronomical Journal*, 158, 228
- Gibson, N. P., Merritt, S., Nugroho, S. K., et al. 2020, *Monthly Notices of the Royal Astronomical Society*, 493, 2215

- Gibson, N. P., Nugroho, S. K., Lothringer, J., Maguire, C., & Sing, D. K. 2022, *Monthly Notices of the Royal Astronomical Society*, 512, 4618
- Gordon, I. E., Rothman, L. S., Hargreaves, e. R., et al. 2022, *Journal of quantitative spectroscopy and radiative transfer*, 277, 107949
- Grasser, N., Snellen, I. A., Landman, R., Picos, D. G., & Gandhi, S. 2024, *Astronomy & Astrophysics*, 688, A191
- Gray, D. F. 2008, *The Observation and Analysis of Stellar Photospheres*
- Hawker, G. A., Madhusudhan, N., Cabot, S. H., & Gandhi, S. 2018, *The Astrophysical Journal Letters*, 863, L11
- Husser, T.-O., Wende-von Berg, S., Dreizler, S., et al. 2013, *Astronomy & Astrophysics*, 553, A6
- Jindal, A., de Mooij, E. J., Jayawardhana, R., et al. 2020, *The Astronomical Journal*, 160, 101
- Jones, A., Noll, S., Kausch, W., Szyszka, C., & Kimeswenger, S. 2013, *Astronomy & Astrophysics*, 560, A91
- Kasper, D., Bean, J. L., Line, M. R., et al. 2022, *The Astronomical Journal*, 165, 7
- Keles, E., Mallonn, M., Kitzmann, D., et al. 2022, *Monthly Notices of the Royal Astronomical Society*
- Kokori, A., Tsiaras, A., Edwards, B., et al. 2023, *The Astrophysical Journal Supplement Series*, 265, 4
- Kubyskhina, D., Vidotto, A. A., Fossati, L., & Farrell, E. 2020, *Monthly Notices of the Royal Astronomical Society*, 499, 77
- Lafarga, M., Brogi, M., Gandhi, S., et al. 2023, *Monthly Notices of the Royal Astronomical Society*, 521, 1233
- Lockwood, A. C., Johnson, J. A., Bender, C. F., et al. 2014, *The Astrophysical Journal Letters*, 783, L29
- Luhman, K. 2018, *The Astronomical Journal*, 156, 271
- Madhusudhan, N. 2012, *The Astrophysical Journal*, 758, 36
- McKemmish, L. K., Masseron, T., Hoeijmakers, H. J., et al. 2019, *Monthly Notices of the Royal Astronomical Society*, 488, 2836
- Meech, A., Aigrain, S., Brogi, M., & Birkby, J. L. 2022, *Monthly Notices of the Royal Astronomical Society*, 512, 2604
- Molaverdikhani, K., Henning, T., & Mollière, P. 2019, *The Astrophysical Journal*, 883, 194
- Mollière, P., Stolker, T., Lacour, S., et al. 2020, *Astronomy & Astrophysics*, 640, A131
- Mollière, P., van Boekel, R., Dullemond, C., Henning, T., & Mordasini, C. 2015, *The Astrophysical Journal*, 813, 47
- Mollière, P., Wardenier, J., van Boekel, R., et al. 2019, *Astronomy & Astrophysics*, 627, A67
- Mollière, P. M. 2017, PhD thesis
- Morris, B. M., Tollerud, E., Sipińcz, B., et al. 2018, *The Astronomical Journal*, 155, 128
- Nasedkin, E., Mollière, P., & Blain, D. 2024, *The Journal of Open Source Software*, 9, 5875
- Newton, E. R., Mann, A. W., Kraus, A. L., et al. 2021, *The Astronomical Journal*, 161, 65
- Ng, K.-C. 1974, *J. Chem. Phys.*, 61, 2680
- Noll, S., Kausch, W., Barden, M., et al. 2012, *Astronomy & Astrophysics*, 543, A92
- Oh, S., Price-Whelan, A., Hogg, D., Morton, T., & Spergel, D. 2017, *VizieR Online Data Catalog*, 515, J
- Olson, G. L., Auer, L., & Buchler, J. R. 1986, *Journal of Quantitative Spectroscopy and Radiative Transfer*, 35, 431
- Owen, J. E. 2020, *Monthly Notices of the Royal Astronomical Society*, 498, 5030
- Palle, E., Biazzo, K., Bolmont, E., et al. 2025a, *Experimental Astronomy*, 59, 1
- Palle, E., Yan, F., Morello, G., et al. 2025b, *Astronomy & Astrophysics*, 697, A31
- Parker, L. T., Mendonça, J. M., Diamond-Lowe, H., et al. 2025, *Monthly Notices of the Royal Astronomical Society*, 538, 3263
- Peláez-Torres, A., Sánchez-López, A., Nortmann, L., et al. 2025, *Tighter constraints on the atmosphere of GJ 436 b from combined high-resolution CARMENES and CRIFES+ observations*
- Pickles, A. 1998, *Publications of the Astronomical Society of the Pacific*, 110, 863
- Pino, L., Brogi, M., Désert, J., et al. 2022, *A&A*, 668, A176
- Piskunov, N., Kupka, F., Ryabchikova, T., Weiss, W., & Jeffery, C. 1995, *Astronomy and Astrophysics Supplement*, v. 112, p. 525, 112, 525
- Rasmussen, K. C., Currie, M. H., Hagee, C., et al. 2023, *The Astronomical Journal*, 166, 155
- Richard, C., Gordon, I. E., Rothman, L. S., et al. 2012, *Journal of Quantitative Spectroscopy and Radiative Transfer*, 113, 1276
- Ridden-Harper, A., Nugroho, S. K., Flagg, L., et al. 2023, *The Astronomical Journal*, 165, 170
- Ridden-Harper, A., Snellen, I., Keller, C., et al. 2016, *Astronomy & Astrophysics*, 593, A129
- Rodler, F., Lopez-Morales, M., & Ribas, I. 2012, *The Astrophysical Journal Letters*, 753, L25
- Sánchez, S. F., Aceituno, J., Thiele, U., Pérez-Ramírez, D., & Alves, J. 2007, *Publications of the Astronomical Society of the Pacific*, 119, 1186
- Sánchez-López, A. & Millán, A. P. 2025, arXiv preprint arXiv:2501.09494
- Sanna, N., Martins, B. C., Martins, A. d. M., et al. 2024, in *Ground-based and Airborne Instrumentation for Astronomy X*, Vol. 13096, SPIE, 1299–1305
- Smith, P. C., Line, M. R., Bean, J. L., et al. 2024, *The Astronomical Journal*, 167, 110
- Snellen, I. A., De Kok, R. J., De Mooij, E. J., & Albrecht, S. 2010, *Nature*, 465, 1049
- Sousa-Silva, C., Al-Refaie, A. F., Tennyson, J., & Yurchenko, S. N. 2015, *Monthly Notices of the Royal Astronomical Society*, 446, 2337
- Stassun, K. G., Oelkers, R. J., Paegert, M., et al. 2019, *The Astronomical Journal*, 158, 138
- Stock, J. W., Kitzmann, D., Patzer, A. B. C., & Sedlmayr, E. 2018, *Monthly Notices of the Royal Astronomical Society*, 479, 865
- Taberero, H., Allende Prieto, C., Zapatero Osorio, M. R., et al. 2020, *Monthly Notices of the Royal Astronomical Society*, 498, 4222
- Thorngren, D. P., Fortney, J. J., Murray-Clay, R. A., & Lopez, E. D. 2016, *The Astrophysical Journal*, 831, 64
- Tsai, S.-M., Lyons, J. R., Grosheintz, L., et al. 2017, *The Astrophysical Journal Supplement Series*, 228, 20
- Tsai, S.-M., Malik, M., Kitzmann, D., et al. 2021, *The Astrophysical Journal*, 923, 264
- Vach, S., Zhou, G., Huang, C. X., et al. 2024, *The Astronomical Journal*, 167, 210
- Wilks, S. S. 1938, *The annals of mathematical statistics*, 9, 60
- Woitke, P., Helling, C., Hunter, G., et al. 2018, *Astronomy & Astrophysics*, 614, A1
- Zhang, M., Knutson, H. A., Wang, L., et al. 2021, *The Astronomical Journal*, 161, 181

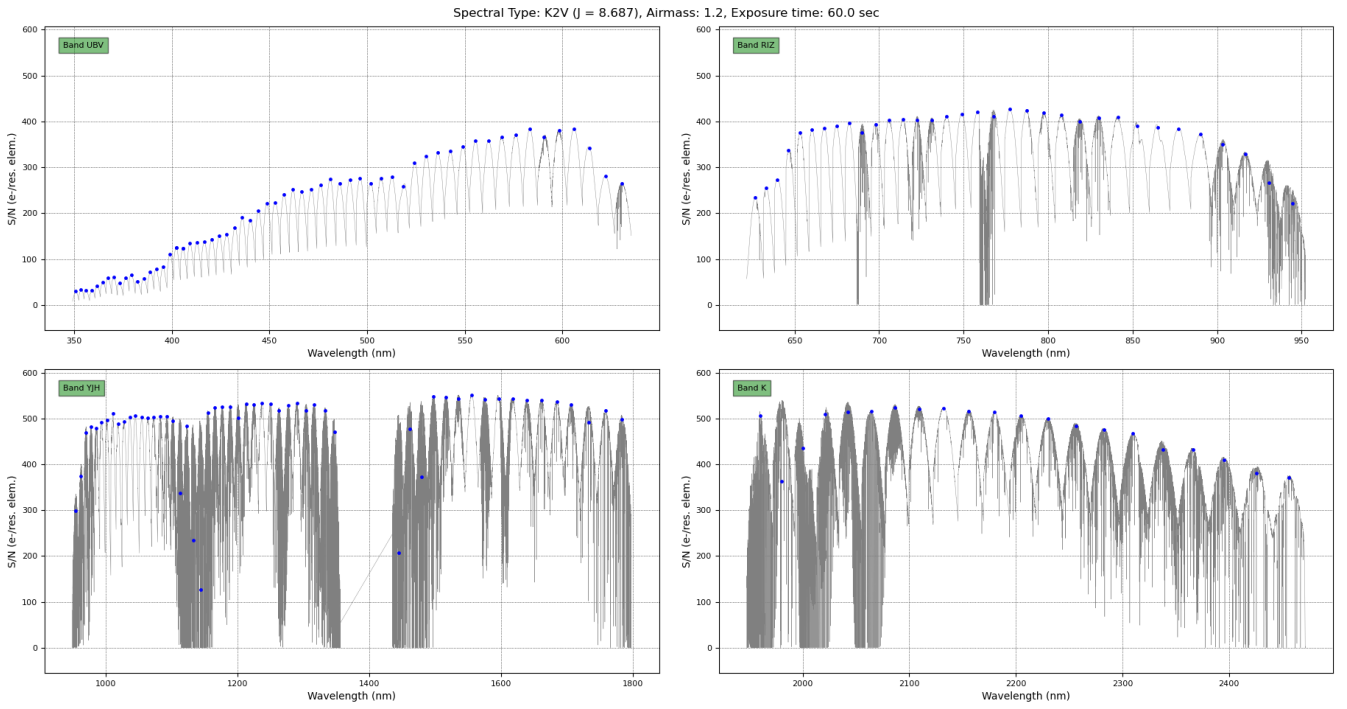


Fig. A.1: The SNR/resolution element across all possible bands for a V1298 Tau like star obtained using the ANDES-ETC simulator (Sanna et al. 2024; Palle et al. 2025b). The exposure time is 60 s and the airmass value assumed to model the transmission of Earth’s atmosphere is 1.2.

Appendix A: Comparison of Ratri with the ANDES exposure time calculator

Appendix B: An example 3-parameter retrieval for V1298 Tau b

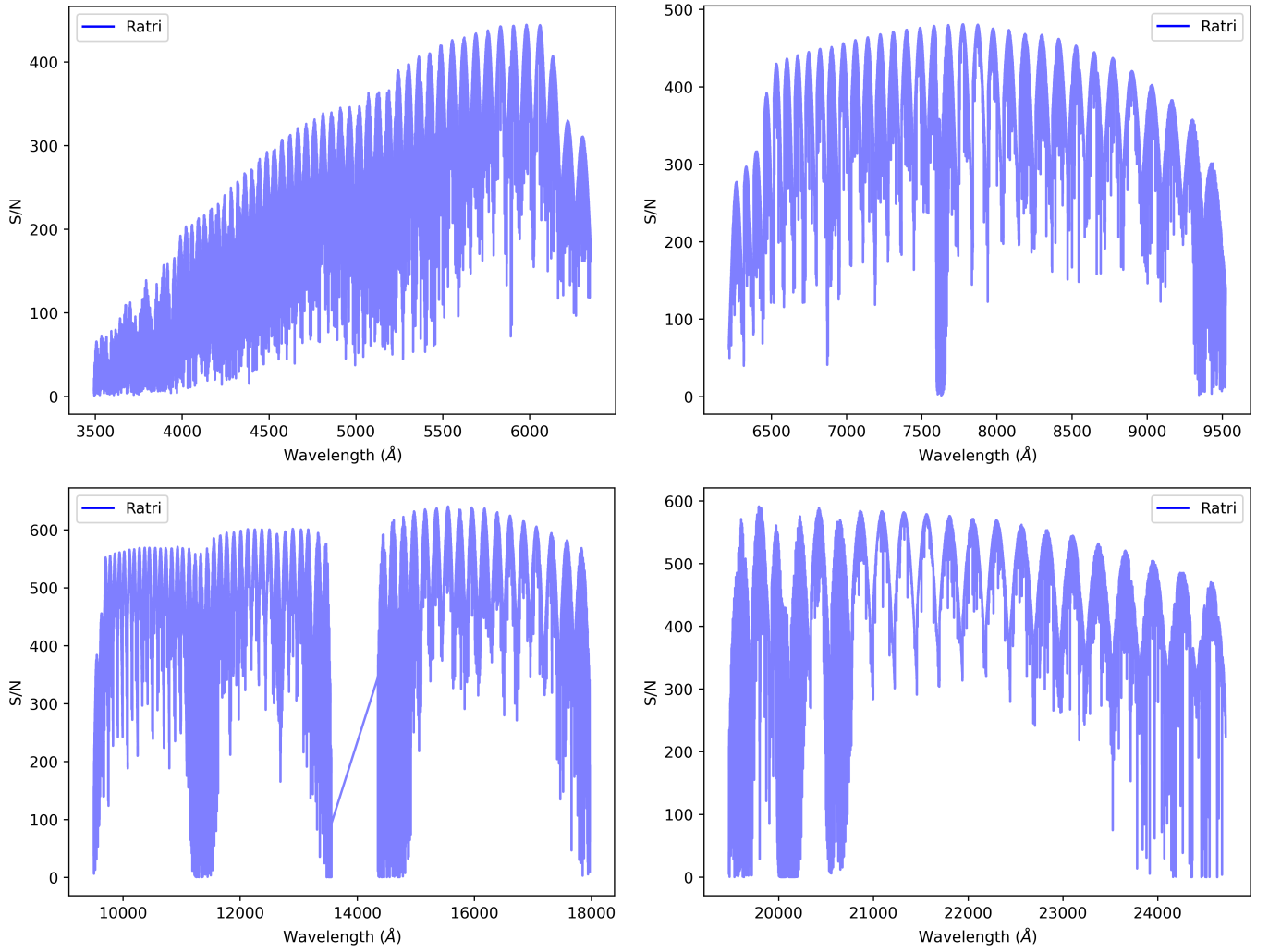


Fig. A.2: The SNR/resolution element for (top-left) Band UBV, (top right) Band RIZ, (bottom left) Band YJH, and (bottom right) Band K for V1298 Tau obtained using Ratri (Dash et al. 2025). The values of the exposure time and airmass are the same as in Figure A.1. While the SNR/resolution element values are slightly over-predicted (by about a factor of 1.1 at the peak values) compared to the values in Figure A.1, the overall trend of the plots remains the same.

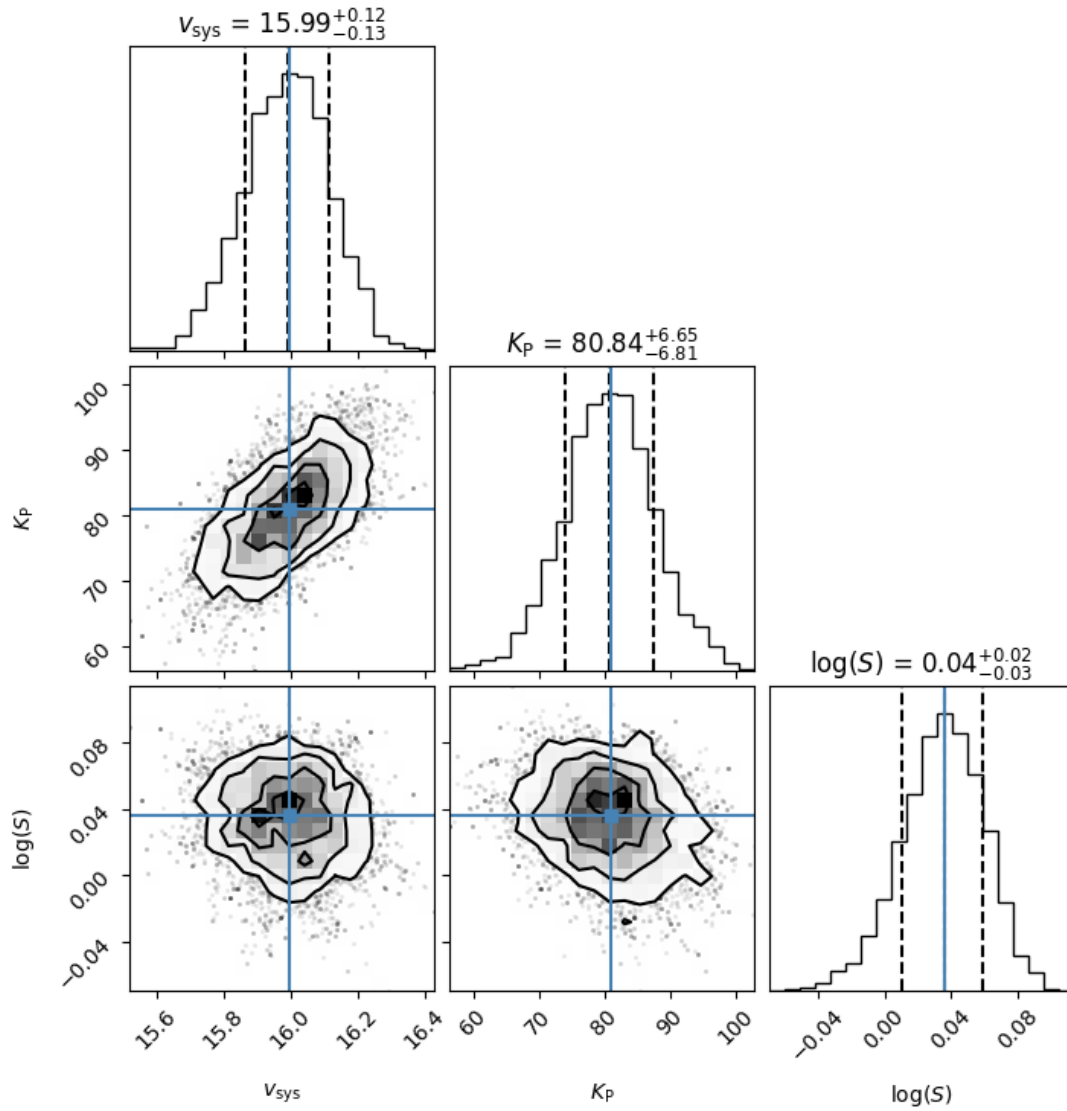


Fig. B.1: A three-component Markov Chain Monte Carlo (MCMC) retrieval of the orbital parameters and cross-correlated template model scale factor for an injected signal of V1298 Tau b from 1000 iterations and using the two simulated nights (Nights 2 and 3) with out-of-transit phases from Section 3.1.1. The template models are reprocessed before cross-correlation. The injected values for v_{sys} and K_p fall within the 1σ contours for their posteriors. The retrieved value of $\log(S) \sim 0$, which motivates our usage of $S = 1$ in Equation 3. The python library `emcee` (Foreman-Mackey et al. 2013) was used to perform these MCMC retrievals.